A&A 647, A50 (2021)
https://doi.org/10.1051/0004-6361/202039206

Astronomy & Astrophysics

Radio halos in a mass-selected sample of 75 galaxy clusters

I. Sample selection and data analysis⋆

V. Cuciti[1], R. Cassano[2], G. Brunetti[2], D. Dallacasa[3,2], R. J. van Weeren[4], S. Giacintucci[9], A. Bonafede[3,2], F. de Gasperin[1], S. Ettori[7,8], R. Kale[5], G. W. Pratt[6], and T. Venturi[2]

[1] Hamburger Sternwarte, Universität Hamburg, Gojenbergsweg 112, 21029 Hamburg, Germany
e-mail: vcuciti@hs.uni-hamburg.de
[2] INAF-Istituto di Radioastronomia, Via P. Gobetti 101, 40129 Bologna, Italy
[3] Dipartimento di Fisica e Astronomia, Università di Bologna, Via P. Gobetti 93/2, 40129 Bologna, Italy
[4] Leiden Observatory, Leiden University, PO Box 9513, 2300 RA Leiden, The Netherlands
[5] National Centre for Radio Astrophysics, Tata Institute of Fundamental Research Savitribai Phule Pune University Campus, Pune 411 007, Maharashtra, India
[6] AIM, CEA, CNRS, Université Paris-Saclay, Université Paris Diderot, Sorbonne Paris Cité, 91191 Gif-sur-Yvette, France
[7] INAF, Osservatorio di Astrofisica e Scienza dello Spazio, Via Pietro Gobetti 93/3, 40129, Bologna, Italy
[8] INFN, Sezione di Bologna, Viale Berti Pichat 6/2, 40127 Bologna, Italy
[9] Naval Research Laboratory, 4555 Overlook Avenue SW, Code 7213, Washington DC 20375, USA

Received 18 August 2020 / Accepted 26 November 2020

ABSTRACT

Context. Radio halos are synchrotron diffuse sources at the centre of a fraction of galaxy clusters. The study of large samples of clusters with adequate radio and X-ray data is necessary to investigate the origin of radio halos and their connection with the cluster dynamics and formation history.
Aims. The aim of this paper is to compile a well-selected sample of galaxy clusters with deep radio observations to perform an unbiased statistical study of the properties of radio halos.
Methods. We selected 75 clusters with $M \geq 6 \times 10^{14} M_{\odot}$ at $z = 0.08-0.33$ from the *Planck* Sunyaev-Zel'dovich catalogue. Clusters without suitable radio data were observed with the Giant Metrewave Radio Telescope and/or the *Jansky* Very Large Array to complete the information about the possible presence of diffuse emission. We used archival *Chandra* X-ray data to derive information on the clusters' dynamical states.
Results. This observational campaign led to the detection of several cluster-scale diffuse radio sources and candidates that deserve future follow-up observations. Here we summarise their properties and add information resulting from our new observations. For the clusters where we did not detect any hint of diffuse emission, we derived new upper limits to their diffuse flux.
Conclusions. We have built the largest mass-selected (>80% complete in mass) sample of galaxy clusters with deep radio observations available to date. The statistical analysis of the sample, which includes the connection between radio halos and cluster mergers, the radio power – mass correlation, and the occurrence of radio halos as a function of the cluster mass, will be presented in Paper II.

Key words. galaxies: clusters: general – galaxies: clusters: intracluster medium – radiation mechanisms: non-thermal

1. Introduction

Clusters of galaxies occupy an exclusive position in the cosmic hierarchy since they are the most massive gravitationally bound structures in the Universe. They form and grow at the intersection of cosmic filaments, where smaller systems are channelled by the gravitational field that is dominated by dark matter. Mergers between clusters are the most energetic events in the Universe. Most of this energy contributes to heat the intracluster medium (ICM) up to the observed temperature (10^7-10^8 K). At the same time, a fraction of this energy, is channelled into the acceleration of particles and amplification of magnetic fields in the ICM by complex mechanisms, presumably invoking turbulence and shocks operating in plasma with unique properties (Brunetti & Jones 2014). This creates diffuse cluster-scale synchrotron emission, which has been observed in a growing number of clusters. Depending on their size and location, these sources are classified as radio relics or radio halos (see van Weeren et al. 2019, for a review). Radio relics are elongated, often arc-shaped, sources located at the periphery of dynamically disturbed clusters. They are considered as tracers of merger-driven shocks propagating through the ICM (e.g. Ensslin et al. 1998; Markevitch et al. 2005; Kang et al. 2012; Pinzke et al. 2013). Moreover, some relaxed clusters host mini halos, confined within the core, generally on scales $<0.2 \times R_{500}$ (Giacintucci et al. 2008, 2017, 2019). The mechanisms responsible for the formation of mini halos are still a matter of debate, possibilities include electrons re-acceleration by turbulence generated in the core by several mechanisms (Gitti et al. 2002; ZuHone et al. 2013) and secondary particles generated by hadronic collisions in the ICM (e.g. ZuHone et al. 2015; Pfrommer & Enßlin 2004; Jacob & Pfrommer 2017).

⋆ The reduced images are only available at the CDS via anonymous ftp to cdsarc.u-strasbg.fr (130.79.128.5) or via http://cdsarc.u-strasbg.fr/viz-bin/cat/J/A+A/647/A50

This work is mainly focused on radio halos, which are centrally located sources whose emission is roughly coincident with the X-ray emission of the host clusters. In the current theoretical scenario, radio halos form via the turbulent re-acceleration of electrons in the ICM (Brunetti et al. 2001; Petrosian 2001; Brunetti & Lazarian 2007, 2011, 2016; Pinzke et al. 2017). The basic idea is that such turbulence is injected into the ICM during merging events. As a consequence, a strong connection between the properties of radio halos and the cluster mass and dynamical state is expected. Radio halos should be preferentially found in massive, merging clusters, should be rare in small and less disturbed systems, and should absent in relaxed clusters. Less energetic merger events are expected to form radio halos with very steep spectra ($\alpha < -1.5$, with $S(\nu) \propto \nu^{\alpha}$), the so-called ultra steep spectrum radio halos (USSRHs, e.g. Brunetti et al. 2008).

The study of the statistical properties of radio halos in galaxy clusters is a powerful tool to investigate the connection and evolution of these sources with the cluster dynamics and formation history and to test theoretical models for their formation. Pioneering studies using Arecibo, the NVSS and the WENNS surveys (Hanisch 1982; Andernach et al. 1986; Giovannini et al. 1999; Kempner & Sarazin 2001) revealed that radio halos are not ubiquitous in galaxy clusters and that their occurrence increases with increasing the X-ray luminosity of the host clusters (Liang et al. 2000), although the role of selection biases due to the sensitivity limit of the used surveys was unclear (Kempner & Sarazin 2001; Rudnick et al. 2006). In this respect, an important step forwards has been achieved with the Giant Meterwave Radio Telescope (GMRT) radio halo survey (Venturi et al. 2007, 2008) and its extension (Kale et al. 2013, 2015). That work led to the discovery of the so-called radio 'bimodality' of galaxy clusters. Indeed radio halos are found in merging systems and follow the correlation between the radio power and the X-ray luminosity of the host cluster, while relaxed clusters without radio halos lie well below that correlation (Brunetti et al. 2009; Cassano et al. 2010). All these studies were based on the selection of the most X-ray luminous clusters, while the key parameter for the formation of radio halos is the cluster mass. The advent of clusters surveys via the Sunyaev-Zel'dovich (SZ) effect offers the opportunity to compile nearly mass selected samples of clusters with high levels of completeness (Basu 2012; Cassano et al. 2013; Cuciti et al. 2015; Knowles et al. 2019), owing to the tight correlation between the SZ effect and the cluster mass (Motl et al. 2005; Nagai 2006). The first results based on SZ selected samples of clusters suggested that the fraction of radio halos is larger with respect to X-ray selected samples (Sommer & Basu 2014). Cassano et al. (2013) showed that clusters are bimodal behaviour also in the radio luminosity–mass diagram.

With the aim of performing the first unbiased census of radio halos in a mass-selected sample of galaxy clusters, we selected 75 massive clusters from the *Planck* SZ catalogue (Planck Collaboration XXIX 2014). The first results on the occurrence of radio halos, based on a sub-sample of clusters that had available radio information, were presented in Cuciti et al. (2015). We showed that the fraction of radio halos drops in low mass clusters, in line with turbulent re-acceleration models. However, that result could be affected by the incompleteness of the radio information for the total sample. Therefore, we carried out an observational campaign with the GMRT and the *Jansky* Very Large Array (JVLA) to complete the information about the possible presence of diffuse emission for all the clusters of the sample. In this paper we present the results of these new observations and we summarise the properties of the total sample, both from the radio and the X-ray points of view.

In Sect. 2 we present the selection of the sample, in Sect. 3 we describe the procedures adopted to reduce the radio data and in Sect. 4 we show the results of the radio data analysis. We derive upper limits to the radio emission of clusters without radio halos in Sect. 5. In Sect. 6, we derive the surface brightness radial profile of radio halos. The analysis of the X-ray data is described in Sect. 7 and the dynamical properties of the clusters are discussed in Sect. 8. In Sect. 9 we summarise the work and give our conclusions. We perform the statistical analysis of the radio and X-ray properties of the cluster of this sample in Cuciti et al. (2021, hereafter Paper II).

Throughout this paper we assume a ΛCDM cosmology with $H_0 = 70\,\mathrm{km\,s^{-1}\,Mpc^{-1}}$, $\Omega_\Lambda = 0.7$ and $\Omega_\mathrm{m} = 0.3$.

2. Sample selection

In Cuciti et al. (2015), we selected a sample of massive objects from the *Planck* SZ cluster catalogue (Planck Collaboration XXIX 2014). The selection criteria are discussed in Cuciti et al. (2015) and are summarised below.

At redshift $0.08 < z < 0.2$ we adopted M_{500}[1] $\geq 5.7 \times 10^{14}\,M_\odot$ and we selected clusters observed in the NVSS ($\delta > -40°$, Condon et al. 1998). The lower redshift limit ($z > 0.08$) is driven by the fact that radio interferometers suffer from the lack of sampling at short baselines, resulting in decreased sensitivity to emission on large spatial scales, such as the typical scales of radio halos. Moveover, the largest angular scale detectable with the JVLA at 1.5 GHz (C and D configuration) is 970 arcsec, meaning that at redshift $z < 0.08$ only scales smaller than 1.5 Mpc can be recovered.

At redshift $0.2 < z < 0.33$ we selected clusters with $M_{500} \geq 6 \times 10^{14}\,M_\odot$ and we adopted a declination limit $\delta > -31°$ and $|b| \geq 20°$ ($|b|$ is the galactic latitude), which coincides with that of the GMRT radio halo Survey (Venturi et al. 2007, 2008; Kale et al. 2013, 2015), in order to maximise the availability of information in the literature. The upper redshift limit ($z < 0.33$) is mainly related to the insufficient completeness of the PSZ1 catalogue at higher redshift for these masses.

We adopted a slightly different cut in mass in the two redshift bins to increase the statistics and, at the same time, assure about the same mass completeness of the sample in both redshift ranges (Planck Collaboration XXIX 2014; Cuciti et al. 2015). Indeed, in the selected mass ranges, the completeness of the *Planck* catalogue is ∼90% at $z < 0.2$ and ∼80% at $z > 0.2$, thus we estimated a completeness of our sample of ∼83%[2]. Our sample consists of 75 clusters (21 at $z < 0.2$ and 54 at $z > 0.2$), whose properties are listed in Table 1 and the mass and redshift distributions are shown in Fig. 1. The median redshift of the sample is 0.23. The redshift distribution is rather uniform, except for the very low-redshift tail, where the volume of the Universe is too small to host such massive objects. As expected, the mass distribution is peaked around the mass cut of the sample and then it declines with increasing mass (e.g. Press & Schechter 1974). The median value for the mass is $\sim 7 \times 10^{14}\,M_\odot$. Only a few clusters with $M_{500} \gtrsim 9 \times 10^{14}\,M_\odot$ are present in the Universe at the redshifts considered here.

[1] M_{500} is the mass enclosed in a sphere with radius R_{500}, which is defined as the radius within which the mean mass over-density of the cluster is 500 times the cosmic critical density at the cluster redshift.
[2] Estimated as $\frac{0.9\times21+0.8\times54}{75}$.

Table 1. Total sample clusters properties.

Cluster name	RA	Dec	z	M_{500} ($10^{14}\,M_\odot$)	R_{500} (kpc)	Radio info	$P_{1.4\,\mathrm{GHz}}$ ($10^{24}\,\mathrm{W\,Hz^{-1}}$)
A1437	12 00 22.3	+03 20 33.9	0.134	$5.68^{0.38}_{0.39}$	1200	No RH$^{(*)}$	–
A2345	21 27 06.8	−12 07 56.0	0.176	$5.71^{0.46}_{0.49}$	1190	UL$^{(4)}$	<0.38
A2104	15 40 08.2	−03 18 23.0	0.153	$5.91^{0.57}_{0.60}$	1200	UL$^{(*)}$	<0.24
Zwcl 2120.1+2256	21 22 27.1	+23 11 50.3	0.143	$5.91^{0.33}_{0.34}$	1200	RH(c)$^{(*)}$	–
RXC J0616.3−2156	06 16 22.8	−21 56 43.4	0.171	$5.93^{0.43}_{0.45}$	1200	UL$^{(*)}$	<0.25
A1413	11 55 18.9	+23 24 31.0	0.143	$5.98^{0.38}_{0.40}$	1220	MH$^{(5)}$	–
A1576	12 37 59.0	+63 11 26.0	0.302	$5.98^{0.48}_{0.50}$	1160	UL$^{(6)}$	<0.64
A2697	00 03 11.8	−06 05 10.0	0.232	$6.01^{0.58}_{0.61}$	1190	UL$^{(2)}$	<0.41
Z5247	12 33 56.1	+09 50 28.0	0.229	$6.04^{0.56}_{0.59}$	1190	RH(c)$^{(7)}$	–
Zwcl 0104.9+5350	01 07 54.0	+54 06 00.0	0.107	$6.06^{0.41}_{0.43}$	1240	RH$^{(8)}$	1.62 ± 0.15
RXC J0142.0+2131	01 42 02.6	+21 31 19.0	0.280	$6.07^{0.77}_{0.83}$	1170	RH$^{(40),US(c)}$	0.42 ± 0.01
A1423	11 57 22.5	+33 39 18.0	0.214	$6.09^{0.49}_{0.51}$	1200	UL$^{(2)}$	<0.38
ZwCl 1028.8+1419	10 31 28.2	+14 03 34.0	0.310	$6.11^{0.65}_{0.69}$	1160	No RH$^{(*)}$	–
A3041	02 41 22.1	−28 38 13.0	0.230	$6.12^{0.54}_{0.57}$	1190	RH(c)$^{(*)}$	–
RXC J2051.1+0216	20 51 08.0	+02 15 55.0	0.320	$6.13^{0.69}_{0.74}$	1150	UL$^{(*)}$	<0.73
A2472	22 41 50.6	+17 31 43.0	0.310	$6.15^{0.72}_{0.78}$	1160	UL$^{(*)}$	<1.0
A2895	01 18 11.1	−26 58 23.0	0.230	$6.15^{0.52}_{0.55}$	1190	UL$^{(*)}$	<0.5
RXC J1314.4–2515	13 14 28.0	−25 15 41.0	0.244	$6.15^{0.69}_{0.73}$	1190	RH$^{(1),US(c)}$	0.68 ± 0.24
A2537	23 08 23.2	−02 11 31.0	0.297	$6.17^{0.62}_{0.66}$	1170	UL$^{(2)}$	<0.45
A68	00 37 05.3	+09 09 11.0	0.255	$6.19^{0.64}_{0.68}$	1190	UL$^{(7)}$	<0.42
A56	00 33 50.4	−07 47 28.0	0.300	$6.20^{0.69}_{0.73}$	1170	UL$^{(*)}$	<1.2
A1682	13 06 49.7	+46 32 59.0	0.226	$6.20^{0.45}_{0.46}$	1200	RH(c)$^{(2)}$	–
A1132	10 58 19.6	+56 46 56.0	0.134	$6.23^{0.31}_{0.31}$	1240	RH$^{(27),US}$	0.16 ± 0.08
RXJ1720.1+2638	17 20 10.1	+26 37 29.5	0.164	$6.34^{0.38}_{0.40}$	1240	MH+USSRH$^{(9,40)}$	–
A781	09 20 23.2	+30 26 15.0	0.295	$6.35^{0.58}_{0.61}$	1180	UL$^{(2)}$	<0.36
A384	02 48 13.9	−02 16 32.0	0.240	$6.38^{0.58}_{0.61}$	1210	UL$^{(*)}$	<0.74
A2218	16 35 51.6	+66 12 39.0	0.171	$6.41^{0.26}_{0.26}$	1240	RH$^{(3)}$	0.44 ± 0.10
A3411	08 41 55.6	−17 29 35.7	0.169	$6.48^{0.37}_{0.38}$	1250	RH$^{(10)}$	0.27 ± 0.1
Zwcl 0634.1+4750	06 38 02.5	+47 47 23.8	0.174	$6.52^{0.43}_{0.45}$	1250	RH$^{(25)}$	0.31 ± 0.02
RXC J1322.8+3138	13 22 48.8	+31 39 17.0	0.310	$6.63^{0.59}_{0.62}$	1190	No RH$^{(*)}$	–
A3888	22 34 26.8	−37 44 19.1	0.151	$6.67^{0.33}_{0.34}$	1260	RH$^{(*,33)}$	1.90 ± 0.20
A3088	03 07 04.1	−28 40 14.0	0.254	$6.71^{0.55}_{0.58}$	1220	UL$^{(2)}$	<0.43
A220	01 37 19.5	+07 56 16.0	0.330	$6.74^{0.85}_{0.92}$	1190	UL$^{(*)}$	<0.97
A2667	23 51 40.7	−26 05 01.0	0.226	$6.81^{0.47}_{0.49}$	1240	MH$^{(28)}$	–
A521	04 54 09.1	−10 14 19.0	0.248	$6.90^{0.61}_{0.64}$	1240	RH$^{(11),US}$	1.45 ± 0.13
A2355	21 35 22.5	+01 23 26.0	0.230	$6.92^{0.49}_{0.51}$	1240	UL$^{(*)}$	<0.83
A2631	23 37 40.6	+00 16 36.0	0.278	$6.97^{0.58}_{0.62}$	1230	UL$^{(2)}$	<0.41
A1914	14 26 03.0	+37 49 32.0	0.171	$6.97^{0.35}_{0.36}$	1280	No RH$^{(35)}$	–
RXC J1504.1–0248	15 04 07.7	−02 48 18.0	0.215	$6.98^{0.57}_{0.60}$	1330	MH$^{(13)}$	–
A1733	13 27 03.7	+02 12 15.0	0.260	$7.05^{0.62}_{0.65}$	1240	UL$^{(*)}$	<0.53
A520	04 54 19.0	+02 56 49.0	0.203	$7.06^{0.56}_{0.58}$	1270	RH$^{(14)}$	2.45 ± 0.18
A478	04 13 20.7	+10 28 35.0	0.088	$7.06^{0.35}_{0.36}$	1320	MH$^{(15,40)}$	–
A773	09 17 59.4	+51 42 23.0	0.217	$7.08^{0.44}_{0.46}$	1260	RH$^{(14)}$	1.48 ± 0.16

Notes. RH = Radio Halo, MH = Mini Halo, UL = Upper Limit, US = Ultra Steep, c = candidate. $P_{1.4\,\mathrm{GHz}}$ = k-corrected radio power at 1.4 GHz.
References. $^{(*)}$This paper, $^{(1)}$Venturi et al. (2007), $^{(2)}$Venturi et al. (2008), $^{(3)}$Giovannini & Feretti (2000), $^{(4)}$Bonafede et al. (2017) $^{(5)}$Govoni et al. (2009), $^{(6)}$Kale et al. (2013), $^{(7)}$Kale et al. (2015), $^{(8)}$van Weeren et al. (2011), $^{(9)}$Giacintucci et al. (2014a), $^{(10)}$van Weeren et al. (2013), $^{(11)}$Brunetti et al. (2008), $^{(12)}$Bacchi et al. (2003), $^{(13)}$Giacintucci et al. (2011a), $^{(14)}$Govoni et al. (2001), $^{(15)}$Giacintucci et al. (2014b), $^{(16)}$Giacintucci & Venturi (2009), $^{(17)}$Giovannini et al. (2006), $^{(18)}$Giacintucci et al. (2011b), $^{(19)}$Murgia et al. (2009), $^{(20)}$Vacca et al. (2011), $^{(21)}$Reid et al. (1999), $^{(22)}$Giacintucci et al. (2013), $^{(23)}$Feretti et al. (2001), $^{(24)}$Farnsworth et al. (2013), $^{(25)}$Cuciti et al. (2018), $^{(26)}$Cassano et al. (2013), $^{(27)}$Wilber et al. (2018), $^{(28)}$Giacintucci et al. (2017), $^{(29)}$Savini et al. (2018), $^{(30)}$Sommer et al. (2017), $^{(31)}$Bonafede et al. (2015), $^{(32)}$Venturi et al. (2017), $^{(33)}$Shakouri et al. (2016a), $^{(34)}$ Savini et al. (2019), $^{(35)}$Mandal et al. (2019), $^{(p)}$Ferrari et al. (priv. comm.).

Table 1. continued.

Cluster name	RA	Dec	z	M_{500} ($10^{14}\,M_\odot$)	R_{500} (kpc)	Radio info	$P_{1.4\,\mathrm{GHz}}$ ($10^{24}\,\mathrm{W\,Hz^{-1}}$)
PSZ1 G019.12+3123	16 36 29.4	+03 08 51.0	0.280	$7.08^{0.63}_{0.67}$	1230	UL$^{(*)}$	<0.63
PSZ1 G139.61+24.20	06 22 13.9	+74 41 39.0	0.270	$7.09^{0.56}_{0.58}$	1210	MH+USSRH$^{(28,29)}$	–
A1351	11 42 30.8	+58 32 20.0	0.322	$7.14^{0.51}_{0.53}$	1210	RH$^{(16)}$	9.30 ± 1.5
A115	00 55 59.5	+26 19 14.0	0.197	$7.21^{0.50}_{0.52}$	1280	No RH$^{(14)}$	–
A402	02 57 41.1	−22 09 18.0	0.320	$7.20^{0.65}_{0.68}$	1220	MH (c)$^{(*)}$	–
A1451	12 03 16.2	−21 32 12.7	0.199	$7.32^{0.47}_{0.48}$	1290	RH$^{(25)}$	0.64 ± 0.07
RXCJ 0510.7–0801	05 10 47.9	−08 01 06	0.220	$7.36^{0.61}_{0.63}$	1280	No RH$^{(7)}$	–
PSZ1 G205.07–6294	02 46 27.5	−20 32 5.29	0.310	$7.37^{0.63}_{0.66}$	1240	No RH$^{(p)}$	–
A2261	17 22 17.1	+32 08 02.0	0.224	$7.39^{0.45}_{0.46}$	1280	RH$^{(30,34),US(c)}$	0.68 ± 0.07
RXCJ2003.5–2323	20 03 30.4	−23 23 05.0	0.317	$7.48^{0.64}_{0.67}$	1240	RH$^{(1)}$	10.71 ± 1.73
A2552	23 11 26.9	+03 35 19.0	0.300	$7.53^{0.59}_{0.62}$	1250	RH(c)$^{(7)}$	–
MACS J2135-010	21 35 12.1	−01 02 58.0	0.330	$7.57^{0.61}_{0.64}$	1240	UL$^{(*)}$	<1.17
A3444	10 23 50.8	−27 15 31.0	0.254	$7.62^{0.53}_{0.56}$	1270	MH$^{(7,28)}$	–
S780	14 59 29.3	−18 11 13.0	0.236	$7.71^{0.60}_{0.63}$	1290	MH$^{(7,28)}$	–
A1443	12 01 27.7	+23 05 18.0	0.270	$7.74^{0.54}_{0.56}$	1270	RH$^{(31)}$	0.91 ± 0.04
A2204	16 32 45.7	+05 34 43.0	0.151	$7.96^{0.37}_{0.38}$	1340	MH$^{(15)}$	–
A1758a	13 32 32.1	+50 30 37.0	0.280	$7.99^{0.44}_{0.46}$	1280	RH$^{(17)}$	5.75 ± 0.98
A209	01 31 53.0	−13 36 34.0	0.206	$8.17^{0.43}_{0.44}$	1330	RH$^{(1)}$	1.99 ± 0.21
A665	08 30 45.2	+65 52 55.0	0.182	$8.23^{0.39}_{0.40}$	1340	RH$^{(3)}$	2.51 ± 0.21
A1763	13 35 17.2	+40 59 58.0	0.228	$8.29^{0.40}_{0.41}$	1320	No RH$^{(2)}$	–
RXC J1514.9–1523	15 14 58.0	−15 23 10.0	0.223	$8.34^{0.53}_{0.55}$	1330	RH$^{(18),US(c)}$	2.39 ± 0.70
A1835	14 01 02.3	+02 52 48.0	0.253	$8.46^{0.55}_{0.57}$	1320	MH$^{(19)}$	-
A2142	15 58 16.1	+27 13 29.0	0.089	$8.81^{0.29}_{0.29}$	1420	RH$^{(24,32),US(c)}$	0.19 ± 0.06
A1689	13 11 29.5	−01 20 17.0	0.183	$8.86^{0.44}_{0.45}$	1380	RH$^{(20)}$	0.95 ± 0.28
A1300	11 31 56.3	−19 55 37.0	0.308	$8.83^{0.59}_{0.62}$	1310	RH$^{(21),US(c)}$	3.80 ± 1.43
A2813	00 43 27.4	−20 37 27.0	0.290	$9.16^{0.53}_{0.55}$	1340	UL$^{(*)}$	<1.4
A2390	21 53 34.6	+17 40 11.0	0.234	$9.48^{0.41}_{0.42}$	1380	No RH$^{(34)}$	–
A2744	00 14 18.8	−30 23 00.0	0.307	$9.56^{0.49}_{0.51}$	1350	RH$^{(14)}$	17.40 ± 0.90
A2219	16 40 21.1	+46 41 16.0	0.228	$11.01^{0.36}_{0.37}$	1450	RH$^{(12)}$	5.63 ± 0.80
PSZ1 G171.96-40.64	03 12 57.4	+08 22 10.0	0.270	$11.13^{0.56}_{0.58}$	1440	RH$^{(22),US(c)}$	4.90 ± 1.35
A697	08 42 53.3	+36 20 12.0	0.282	$11.48^{0.46}_{0.47}$	1190	RH$^{(2),US}$	1.51 ± 0.14
A2163	16 15 46.9	−06 08 45.0	0.203	$16.44^{0.40}_{0.41}$	1680	RH$^{(23)}$	22.90 ± 1.16

3. Radio data analysis

The presence of diffuse radio emission has been already studied with deep radio observations in the literature for 55, out of the 75 clusters of the sample. For three of them, which are known to host diffuse emission, we obtained observations at different frequencies. Overall, in this paper we present new radio observations of the 23 galaxy clusters listed in Table 2. These observations were carried out with the GMRT and/or the JVLA. In particular, we analysed GMRT 610 MHz observations of 11 clusters, GMRT 330 MHz observations of eight clusters and JVLA 1.5 GHz observations of 15 clusters. The details about the radio data analysed here are given in Table 2. The frequency coverage of the sample is heterogeneous, however, this is currently a necessary compromise in order to build a complete sample that is large enough to perform a solid statistical analysis. This limit will be overcome thanks to ongoing surveys with, for example, LOFAR (Shimwell et al. 2019) and MeerKAT (Knowles et al. 2016). We describe the main steps of the data reduction in the following subsections.

3.1. GMRT data analysis

The GMRT observations listed in Table 2 were carried out using an observing bandwidth of 32 MHz subdivided into 256 channels[3]. We reduced these observations with the Astronomical Image Processing System (AIPS) or with the Common Astronomy Software Applications (CASA). Regardless of the software we used, the calibration procedure is essentially the same and it is outlined in the following. The flux density scale was set according to Scaife & Heald (2012). The bandpass was corrected using the flux density calibrators. As a first step we obtained amplitude and gain corrections for the primary calibrators in few central channels free of radio-frequency interference (RFI); these solutions were applied before determining the bandpass in order to remove possible time variations of the gains during the observation. Once we applied the bandpass, gain solutions for all the calibrator sources on the full range of channel were

[3] Only A2104 was observed with the old GMRT setup, namely with the simultaneous observation in two bands, the upper side band and the lower side band, each 16 MHz wide.

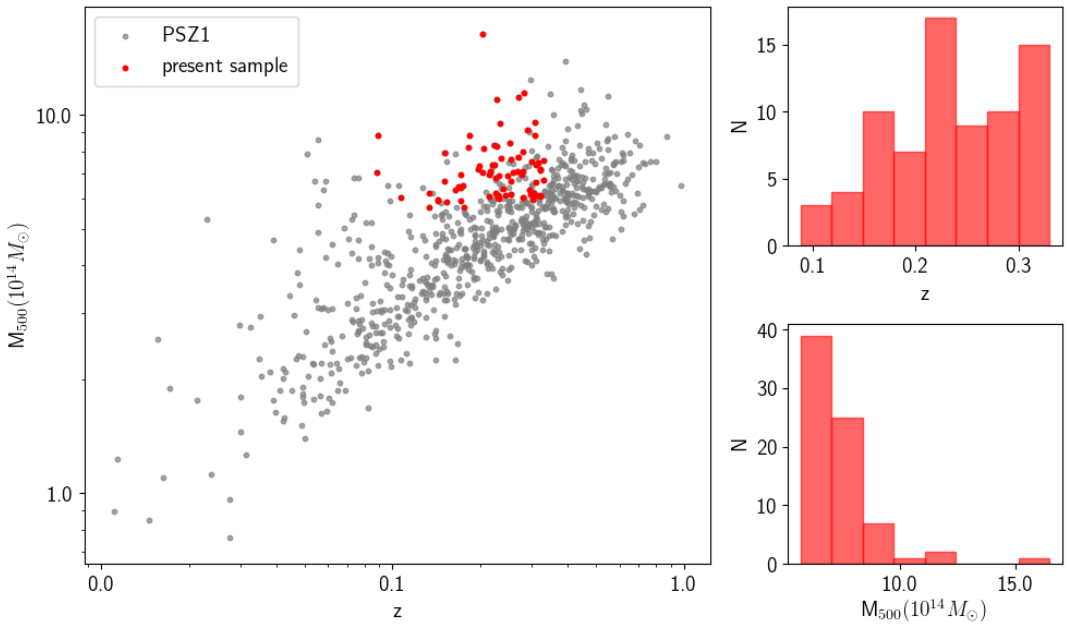

Fig. 1. Mass and redshift distribution of the clusters of the sample. *Left*: distribution of the clusters of the *Planck* SZ cluster catalogue in the $M_{500} - z$ diagram. Clusters belonging to the sample presented here are marked in red. *Top right*: redshift distribution of the clusters of our sample distribution. *Bottom right*: mass distribution of the clusters of our sample.

determined and transferred to the target source. Automatic removal of RFI was performed either with the CASA task `flagdata` or with the AIPS task `RFLAG`. Further manual editing of the data was performed. The central channels were averaged to a smaller number of channels each 1−2 MHz wide to reduce the size of the dataset without introducing significant bandwidth smearing within the primary beam. A number of phase-only self-calibration rounds were carried out on the target field to reduce residual phase variations. A final amplitude and phase self-calibration was applied. Wide field imaging was implemented to account for the non-coplanarity of the baselines. In particular, we used the wprojection algorithm (Cornwell et al. 2005, 2008) in CASA, while in AIPS we subdivided the field of view in tens of facets (the exact number of facets depending on the frequency, the resolution and the presence of bright sources). Facets were imaged separately, with a different phase centre, and then recombined. In CASA, wide band imaging (`mode=mfs`, `nterms=2`) was also used to consider the combination of the sources spectral index and the frequency dependency of the primary beam attenuation. To deal with the bright sources in the field of view that typically reduce the dynamic range of the image we adopted the so called 'peeling' technique. Specifically, we obtained direction-dependent amplitude and phase solutions for those sources and then subtracted them out from the *uv*-data. We did not add the 'peeled' sources back into the final data, however, being typically far from the pointing centre, they are outside the portions of images shown in the paper.

We used the 'Briggs' weighting scheme (Briggs 1995) with `robust=0` throughout the self-calibration[4] and we produced final high-resolution images whose properties are listed in Table 2. The images of the three clusters marked with an asterisks in the column 'telescope' in Table 2, were severely affected by artefacts due to bright sources in the field or residual RFI. To improve their quality, we processed those datasets with the Source Peeling and Atmospheric Modelling (SPAM) pipeline, which is extensively described in Intema et al. (2009, 2017), and Intema (2014).

We subtracted all the compact sources from the *uv*-data. First we made high-resolution images excluding the baselines sensitive to the emission on scales larger than ~250 kpc (`uvrange` < 2−3 klambda depending on the cluster redshift). We subtracted the clean components of the sources detected in the high-resolution images and we used the new dataset to produced low-resolution images. These low-resolution images are more sensitive to the extended low surface brightness emission and thus are suitable to evaluate the presence of sources such as radio halos or relics. Images were corrected for the primary beam response. The uncertainty on the flux scale is estimated to be 10% (e.g. Chandra et al. 2004).

3.2. JVLA data analysis

We performed the data reduction, both calibration and imaging, of the JVLA datasets with CASA. The total bandwidth, from 1 to 2 GHz, is divided into 16 spectral windows, each with 64 channels of 2 MHz in width. In this paper we use 1.5 GHz as the reference frequency for JVLA observations.

As a first step, the data were Hanning smoothed. We applied the pre-determined antenna position offset and elevation-dependent gain tables. The flux density scale was set according to Perley & Butler (2013). We determined amplitude and phase solutions for the flux calibrators in the ten central channels of each spectral window in order to remove possible time variations during the calibrator observation. These solutions were pre-applied to find the delay terms and to correct for the bandpass response. We obtained the complex gain solutions for the calibrator sources on the full bandwidth pre-applying the bandpass and delay solutions. Finally, we applied all the calibration tables to the target fields. Automatic RFI flagging was applied to the target fields using the CASA task `flagdata`. To reduce the

[4] We used `robust=0` both in AIPS and CASA, although we are aware that the definition of the robust parameter is slightly different in the two softwares.

Table 2. Summary of the radio data analysis.

Name	Telescope	Project code	ν (MHz)	Δt (min)	Beam ($''\times''$)	rms (mJy beam^{-1})	Detection
A56	JVLA C	14B-190	1500	40	13.8×10.4	0.080	UL
A2813	JVLA C	14B-190	1500	40	11.4×9.5	0.035	UL
A2895	JVLA C	14B-190	1500	40	14.6×9.0	0.040	UL
A3041	JVLA C	14B-190	1500	40	18.0×8.6	0.035	Candidate RH
A220	JVLA C	14B-190	1500	40	11.6×9.8	0.045	UL
A384	JVLA C	14B-190	1500	40	13.5×10.4	0.035	UL
	GMRT	26_021	610	220	5.9×4.8	0.050	–
Zwcl1028.8+1419	GMRT	27_025	610	330	5.3×4.8	0.056	No UL
RXC J1322.8+3138	GMRT	27_025	610	150	5.7×4.4	0.060	No UL
A1733	GMRT	27_025	610	250	7.9×5.0	0.060	UL
PSZ1 G019.12+3123	GMRT	26_021	610	250	5.0×3.8	0.035	UL
MACS J2135-010	GMRT	30_019	610	300	7.8×5.8	0.080	UL
A2355	JVLA C	14B-190	1500	40	11.6×10.8	0.040	UL
	GMRT	30_019	610	300	8.3×6.1	0.130	–
RXC J2051.1+0216	JVLA C	14B-190	1500	40	14.1×11.5	0.050	UL
	GMRT	26_021	610	200	6.0×4.8	0.100	–
A2472	JVLA C	14B-190	1500	40	10.5×10.1	0.040	UL
PSZ1 G139.61+2420	JVLA C	14B-190	1500	40	10.3×5.1	0.030	
	GMRT[(a)]	27_025+28_077	610	300+300	6.0×5.0	0.030	MH
A1443	JVLA C+D	13A-268	1500	60+90	15.0×12.0	0.020	
	GMRT	27_025	610	150	5.6×4.2	0.050	RH
	GMRT[(b)]	23_020	330	270	8.6×7.3	0.060	
RXC J0510.7–0801	GMRT	23_004	610	330	5.4×4.8	0.200	No UL
	GMRT	23_004	240	330	15.7×13.1	1.200	No UL
A402	GMRT *	22_021	330	400	13.4×8.6	0.100	Candidate MH
	GMRT *	25_018	330	380	57.0×42.0	1.000	
A1437	GMRT	29_001	330	330	9.0×7.4	0.400	No UL
A2104	GMRT	05VKK01	330	350	13.3×10.4	0.130	UL
Zwcl2120.1+2256	JVLA D	15B-035	1500	40	33.0×30.3	0.075	Candidate RH
	GMRT *	23_046	330	250	10.0×9.2	0.100	
RXC J0616.3–2156	JVLA DnC	15B-035	1500	40	55.4×19.9	0.080	UL
A3888	GMRT	28_066	330	260	14.6×8.3	0.300	RH

Notes. Δt = time on source; UL= Upper limit; RH = radio halo; MH= mini halo; No UL = No detection and No UL available; * = processed with SPAM (Intema et al. 2009; Intema 2014; Intema et al. 2017).
References. [(a)]Savini et al. (2018), [(b)]Bonafede et al. (2015).

size of the dataset, we averaged the 48 central channels of each spectral window to six channels and we averaged in time with a time bin of 15 s. We ran several rounds of phase-only self-calibration on each target field and a final amplitude and phase self-calibration to end up the process. The wprojection algorithm was used to take into account the non-coplanar nature of the array. Wide band imaging is crucial when dealing with the 1 GHz bandwidth of the JVLA; therefore, we used three Taylor terms (`nterms=3`) to take the frequency dependence of the brightness distribution into consideration. The imaging process involves the use of clean masks that have been made with the `PyBDSF` package (Mohan & Rafferty 2015). For the self-calibration we used the 'Briggs' weighting scheme with `robust=0` and we made final high-resolution images whose properties are reported reported in Table 2. Then, in order to highlight the possible diffuse emission, we subtracted all the discrete sources with the same technique described in Sect. 3.1 and we produced low-resolution images, using higher values for the `robust` parameter and/or tapering down the long baselines.

Images were corrected for the primary beam attenuation. The absolute flux scale uncertainties are assumed to be within 2.5% (Perley & Butler 2013).

4. Detection of diffuse emission

In the next Sections, we present the three clusters hosting diffuse emission whose discovery has been already reported in dedicated papers. We summarise the properties of these sources and add complementary information that we obtained with our new data. In Sect. 4.4 we discuss clusters hosting candidate diffuse emission. In the following, the errors reported for the diffuse sources take into account the uncertainty associated with the source subtraction, when applicable (see e.g. Cassano et al. 2013).

4.1. Abell 3888

A3888 has a mass $M_{500} = 6.67 \times 10^{14}\, M_{\odot}$ and it is at $z = 0.151$. The dynamical state of A3888 has been debated in the literature (Pratt et al. 2009; Böhringer et al. 2010;

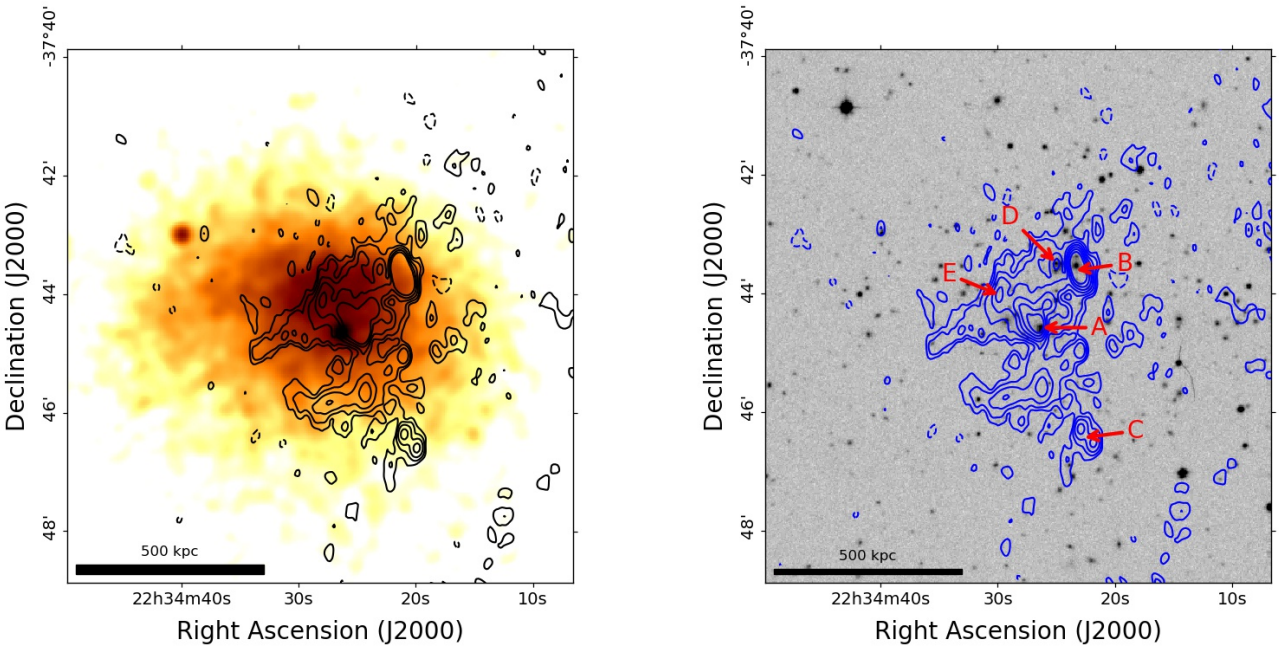

Fig. 2. Images of the cluster A3888. *Left*: X-ray *Chandra* image (colours) with GMRT 33 MHz contours superimposed. Contours start from 0.9 mJy beam^{-1} and are spaced by a factor of two. The −0.9 mJy beam^{-1} contour is dashed. *Right*: same contours as in the left panel superimposed on the optical DSS image. Labels mark the position of discrete radio sources (A to D) and E indicates a patch of diffuse emission with no optical counterpart that we consider to be part of the halo.

Chon et al. 2012; Weißmann et al. 2013; Haarsma et al. 2010). Spectroscopic observations of the member galaxies reveal that they are distributed in two subgroups, suggesting that a merger is ongoing (Shakouri et al. 2016b). Our dynamical analysis, based on the morphological parameters, confirms that A3888 is a merging cluster (Sect. 8). A radio halo in A3888 was discovered with ATCA observations in the frequency range 1.25−2.55 GHz (Shakouri et al. 2016a). The bright radio halo is also detected in our GMRT 330 MHz image (Fig. 2) and its morphology resembles the one described by Shakouri et al. (2016a). The radio emission of the cluster is complex and characterised by the presence of many bright sources embedded in the radio halo emission. As Shakouri et al. (2016a) pointed out, source A[5] and B are head tail member galaxies, while source C is a background radio galaxy. Being diffuse themselves, the subtraction of the head tail galaxies from the visibilities is very difficult. In addition to the compact sources detected in Shakouri et al. (2016a), we detect another patch of emission (labelled E in Fig. 2, right panel) located north-east of source A. The superposition between the radio contours of A3888 and the optical DSS image in shown in Fig. 2. While source A, B and D have clear optical counterparts, the brightest part of E does not have a corresponding galaxy, thus it could be a peak of the radio halo emission. We measured a total flux density of ∼1.29 Jy inside the contours shown in Fig. 2. In order to derive the radio halo flux density we estimated the contribution of the sources embedded in the diffuse emission (except for the patch E) and we subtracted their flux density from the total emission. We obtained a radio halo flux density $S_{330\,\mathrm{MHz}} = 380 \pm 60$ mJy. The LAS of the radio halo, measured from the 3-σ contours, is $190'' \times 160''$ corresponding to a LLS of 500 kpc × 420 kpc.

[5] Source A is actually the blending of two head tail radio galaxies, clearly resolved in the ATCA high-resolution image (Shakouri et al. 2016a).

We note that the comparison between the radio halo flux density at 330 and 1400 MHz would give a very steep spectrum ($\alpha < -1.8$). However, the contribution of the sources embedded in the radio halo is not properly addressed at either frequency and further analysis is necessary to investigate the spectral properties of this radio halo.

4.2. Abell 1443

A1443 is a massive ($M_{500} = 7.74 \times 10^{14}\,M_\odot$) cluster at redshift $z = 0.27$. A radio halo in A1443 has been discovered with GMRT 330 MHz (Bonafede et al. 2015). In addition, the authors detected a peculiar extended source, named 'Γ-shaped' source, and a candidate radio relic on the western side of the cluster. While the 'Γ-shaped' source and the candidate relic are well detected in our GMRT 610 MHz image (not shown here), the radio halo is only marginally visible. We reduced archival JVLA 1.5 GHz observations of A1443, the contours are shown in Fig. 3 (white) and are overlaid on the X-ray *Chandra* image of the cluster. Also at 1.5 GHz, the radio halo is only visible as patches of diffuse emission. We subtracted the compact sources from the *uv*-data and we re-imaged this field at very low-resolution (∼1 arcmin) to increase the possibility of imaging the diffuse emission. The low-resolution contours are shown in cyan in Fig. 3. Although the western part is most likely associated with the residuals of the two extended sources that are particularly challenging to subtract, we are confident that the central part of the diffuse emission belongs to the radio halo. We estimated the flux density of the halo in a region that does not include the two extended sources on the west. The radio halo flux density is $S_{1.5\,\mathrm{GHz}} = 3.5 \pm 0.10$ mJy, corresponding to $P_{1.4\,\mathrm{GHz}} = (9.1 \pm 0.25) \times 10^{23}$ W Hz^{-1}. A1443 has been recently observed with LOFAR at 144 MHz as part of LoTSS (Shimwell et al. 2019). A multi-frequency study including the reanalysis of the 330 MHz GMRT data and the combination with LOFAR data

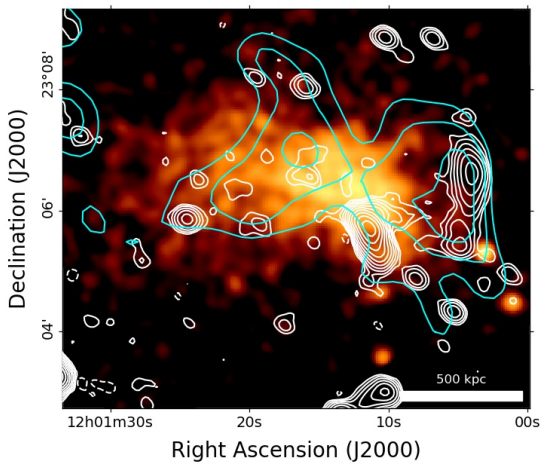

Fig. 3. X-ray *Chandra* image of A1443 with JVLA high-resolution (white) and low-resolution (cyan) contours overlaid. Contours start at 3-σ and are spaced by a factor of two. 1-σ rms noise is 0.02 mJy beam^{-1} with beam = 15″ × 12″ (white contours) and it is 0.08 mJy beam^{-1} with beam = 55″ × 54″ (cyan contours).

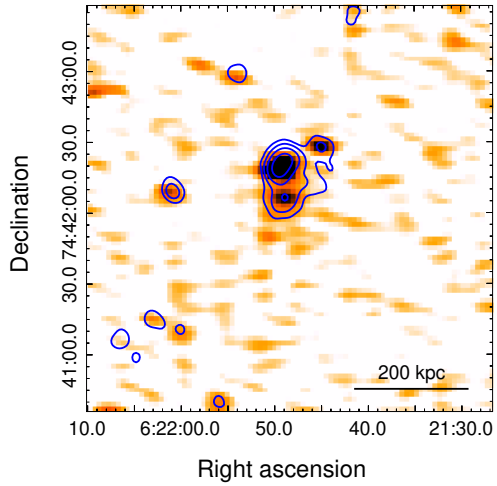

Fig. 4. JVLA C array 10.3″ × 5.1″ resolution image of the center of PSZG139.61+2420 with GMRT 610 MHz contours overlaid. Contours are (±3, 6, 9, 12...)×$\sigma_{\rm rms}$ with $\sigma_{\rm rms}$ = 0.03 mJy beam^{-1} and beam = 7″ × 7″ (Giacintucci et al. 2017).

is ongoing and will be presented in a future paper (Cuciti et al., in prep.).

4.3. PSZG139.61+2420

PSZG139.61+2420 (PSZG139, hereafter) is a low-entropy cool core cluster (Giacintucci et al. 2017) with some trace of dynamical disturbance. Indeed, the X-ray morphology is slightly elongated and the centroid shift parameter has intermediate value between merging and non-merging systems. The mass of PSZG139 is $M_{500} = 7.09 \times 10^{14}\ M_{\odot}$ and the redshift is $z = 0.27$. Two GMRT 610 MHz observations are available for this cluster. Their combination has been presented in Savini et al. (2018) and Giacintucci et al. (2019). We detected three faint discrete sources at the cluster centre, which blend with a diffuse component in the low-resolution image. We classified such a diffuse component as a mini halo (Giacintucci et al. 2019).

PSZG139 has been also observed with LOFAR at 144 MHz. In the LOFAR image the mini halo is surrounded by a larger-scale diffuse component with an estimated spectral index steeper than $\alpha = -1.7$ (Savini et al. 2018). The coexistence of a mini halo in the cool-core with a larger scale, steep spectrum emission, may be the consequence of a minor merger. Diffuse emission with similar properties has bee recently found also in the galaxy cluster RXC J1720.1+2638 (Savini et al. 2019).

In Fig. 4 we present the JVLA 1.5 GHz C array high-resolution image of the central region of PSZG139 compared to the low-resolution GMRT 610 MHz contours (from Giacintucci et al. 2019). At a similar resolution, the mini halo appears less extended towards the west at high frequencies. We subtracted the discrete sources from the *uv*-data and we estimated the flux density of the mini halo in the same region used for the GMRT image (3-σ contours shown in Fig. 4). We obtained a flux density of the mini halo $S_{1.5\,\rm GHz} = 0.60 \pm 0.05$ mJy, in agreement with the value measured with GMRT 1.28 GHz observations by Giacintucci et al. (2019).

4.4. Candidate diffuse emission

4.4.1. Zwcl2120.1+2256

Zwcl2120-1+2256 (Z2120, hereafter) is at $z = 0.143$ and it is one of the less massive clusters in our sample, with $M_{500} = 5.91 \times 10^{14}\ M_{\odot}$. The information available in the literature about this cluster is rather sparse. According to the morphological analysis of the X-ray surface brightness distribution (Sect. 8), we find that Z2120 sits in the intermediate region between merging and relaxed clusters. In fact, the X-ray emission of this cluster is fairly peaked at the centre, but there is a low-surface brightness 'tail' extending to the south-west, suggestive ongoing dynamical activity (Fig. 5, right panel).

The JVLA D array image of Z2120 is shown in Fig. 5 (left panel). In addition to the three compact sources (labelled A, B and C) in the cluster central region, we detected some faint diffuse emission extending towards south-west. The source-subtracted low-resolution image (Fig. 5, right panel) shows some faint residual emission elongated in the NE-SW direction which, interestingly, follows the X-ray emission of the cluster, especially in the southern area. We note that, while the radio emission on top of the peak of the X-ray emission may be partly due to some residuals from the subtracted sources, the emission coincident with the low-surface brightness south-west X-ray tail is not affected by subtraction. The residual flux density measured within the 3-σ contours of Fig. 5 (right panel), considering also the emission in the central region of the cluster, is $S_{1.5\,\rm GHz} \sim 7.7$ mJy. We classify this emission as a candidate radio halo.

We reduced an archival GMRT 330 MHz observation of Z2120 (P.I. C. Jones) with the SPAM pipeline and then we imaged the processed data with CASA. Only some patches of diffuse emission are visible in the cluster central region on the high-resolution image (~10″, Fig. 6, left panel). In the source-subtracted low-resolution image (Fig. 6, right panel) a residual emission of ~46 mJy is detected at low significance level. Remarkably, this emission is spatially coincident with the one detected at higher frequency, thus supporting the idea of a low surface brightness emission associated with the perturbed ICM. Given the low signal to noise ratio of the detection at both frequencies it is difficult to obtain a solid spectral information.

4.4.2. Abell 3041

Abell 3041 is at redshift $z = 0.23$ with mass $M_{500} = 6.12 \times 10^{14}\ M_{\odot}$. An X-ray *Chandra* observation of A3041 is available

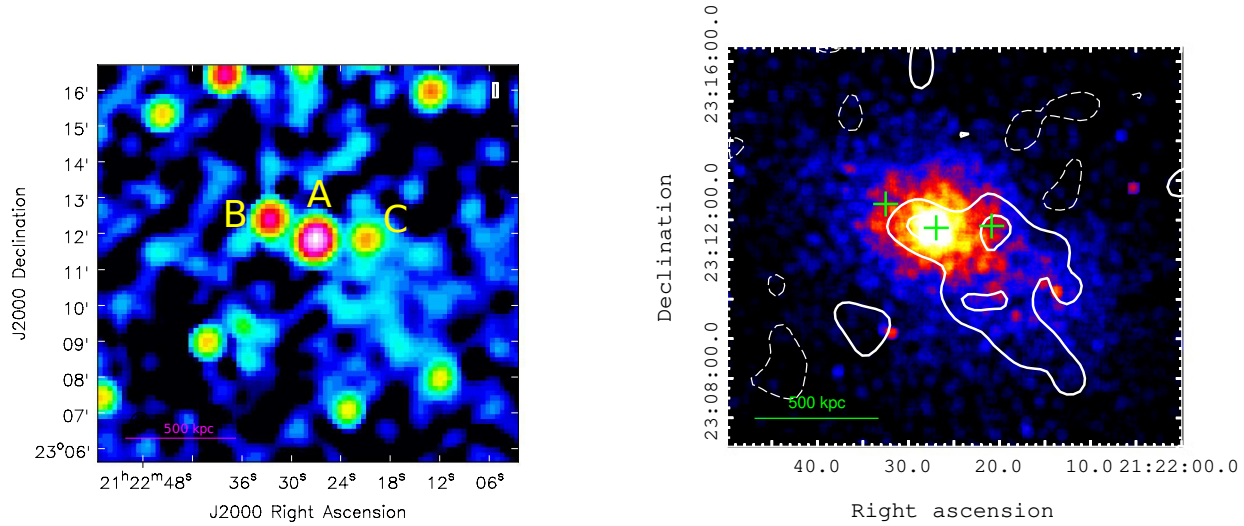

Fig. 5. JVLA image of the cluster Z2120. *Left*: JVLA D array image. The resolution is 33″ × 30″ and the rms noise is 0.06 mJy beam^{-1}. Labels mark the discrete sources in the cluster field. *Right*: low-resolution (55″ × 54″) JVLA contours after the compact sources subtraction overlaid over the X-ray *Chandra* image. Contours are drawn at (3,6...)×σ, with σ = 0.1 mJy beam^{-1}. The 2-σ negative contour is dashed. The green crosses mark the position of the three sources at the cluster centre, which have been subtracted.

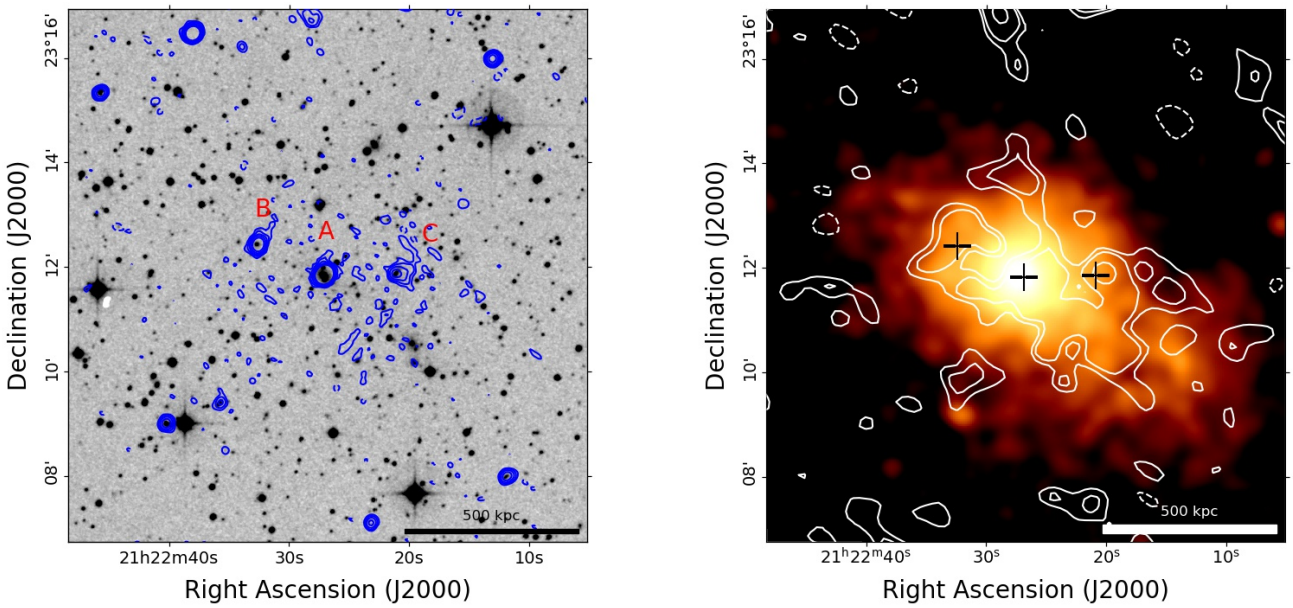

Fig. 6. GMRT images of the cluster Z2120. *Left*: DSS optical image with GMRT high-resolution contours overlaid. Contours start at 0.1 mJy beam^{-1} and are spaced by a factor of two. The first negative contour is dashed. Labels mark the position of discrete sources. *Right*: GMRT 330 MHz low-resolution (32.7″ × 28″) contours after the subtraction of compact sources superimposed on the *Chandra* X-ray image. Contours are (2,3,6...)×σ, with σ = 0.3 mJy beam^{-1}. The position of the discrete sources is marked with a black cross.

in the archive. Although it is very shallow (exposure time 9 ks), we processed and used it to derive the morphological parameters, which place A3041 in the merging region of the morphological diagrams (Sect. 8). In Fig. 7 (left panel) we show a deeper *XMM-Newton* observation that better highlights the disturbed morphology of the cluster.

The cluster hosts two central radio sources, which are blended at the resolution of our C array observation (∼10″). Their overall flux density is 105 ± 3 mJy. Both have optical counterparts in the DSS optical image (Fig. 7, left panel). There is no available redshift for the brightest one, while the fainter one is associated with a member galaxy (Colless et al. 2003). On the eastern side of the cluster there is an FRII radio galaxy extending over ∼5.8 arcmin. The nucleus is located ∼5.5 arcmin from the centre of A3041, and no spectroscopic redshift is available for this source. The host galaxy is detected in the 2 MASS catalogue (Skrutskie et al. 2006), with a K magnitude of 15.62. Using the $K - z$ relation by Willott et al. (2003) we estimated that the redshift of the FRII galaxy is $z = 0.42 \pm 0.16$, suggesting that it may be a background giant radio galaxy extending over almost 2 Mpc.

We subtracted all the discrete sources from the dataset, except for the FRII galaxy. We paid special attention to the subtraction of the two central sources. In particular, we did not adopt the usual approach described in Sect. 3.1, but we subtracted a model made using the whole *uv*-range. In this way, we made

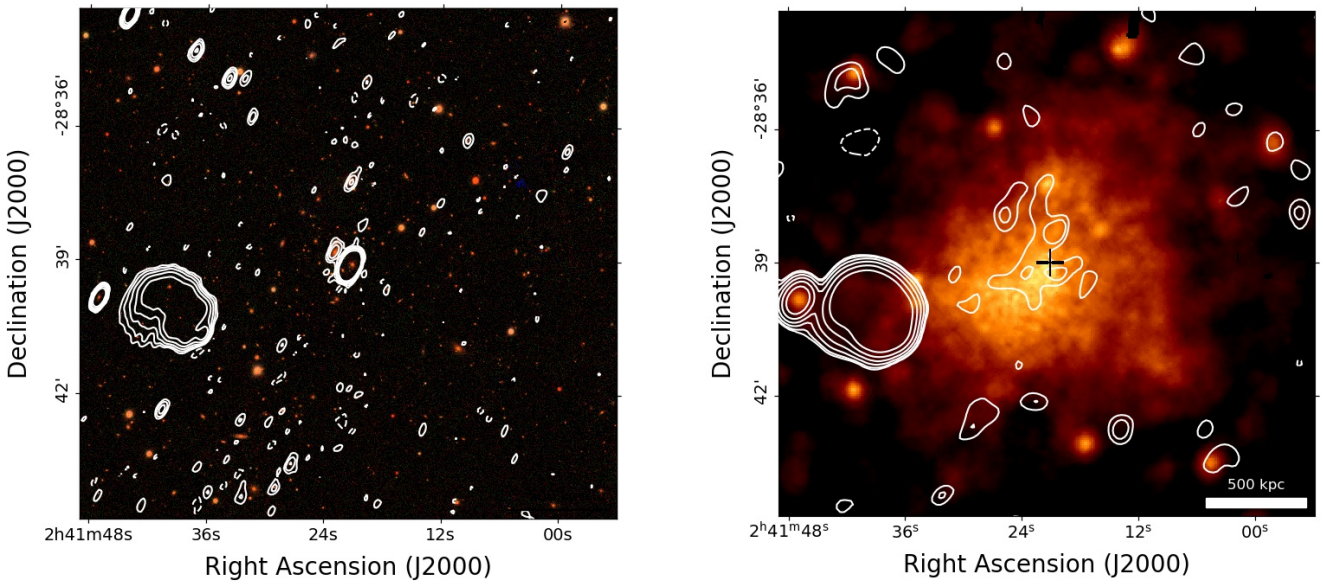

Fig. 7. Images of the cluster A3041. *Left*: high-resolution JVLA C array contours (red) superimposed on the PanSTARRS optical image. Contours start at 0.1 mJy beam^{-1} and are spaced by a factor of two. The first negative contour is dashed. *Right*: X-ray *XMM-Newton* image with low-resolution (35.8″ × 25.5″) JVLA C array contours overlaid. Contours are $(\pm 2, 3, 6...) \times \sigma_{\rm rms}$ with $\sigma_{\rm rms} = 0.08$ mJy beam^{-1}. The discrete sources in the field are subtracted, except for the region of the FRII radio galaxy. The black cross marks the position of the central brightest radio source.

sure that, if there is some faint extended radio emission associated with the central sources, it is subtracted from the data that we then use to produce the low-resolution image, shown in Fig. 7 (right panel). A residual emission of ∼4 mJy is present at the cluster X-ray peak, mostly detected at the 2-σ level only. The spatial coincidence between the thermal and non-thermal emission may suggest that these residuals belong to a cluster diffuse radio source. However, the detection is marginal and we are aware that even a small calibration error around the bright central source might leave some residuals showing up in the low-resolution image. We thus consider A3041 as a case of candidate diffuse emission.

4.4.3. Abell 402

Abell 402 is a massive ($M_{500} = 7.21 \times 10^{14}\, M_\odot$) cluster of galaxies at $z = 0.32$. Its temperature within R_{2500} measured on the [0.7–7] keV band excluding the central 70 kpc region is $8.0^{+1.1}_{-0.9}$ keV (Cavagnolo et al. 2008; Giacintucci et al. 2017). Although the X-ray morphology of the cluster is fairly regular and peaked at the center, the central entropy floor of A402 is relatively high ($K_0 = 156 \pm 25$ keV cm^{-2}, Cavagnolo et al. 2009; Giacintucci et al. 2017) suggesting that it does not possess a cool core and some sort of dynamical activity may be taking place in this cluster.

There are two archival GMRT 330 MHz observations available for this cluster (Obs No: 6153, P.I.: G. Macario and Obs No: 6837, P.I.: A. Bonafede). Both have been processed with the SPAM pipeline and both show evidence of diffuse emission at the cluster center. From the combination of the two images, Giacintucci et al. (2017) classified the diffuse emission in A402 as a candidate radio halo. The images of A402 are shown in Fig. 8. On the left panel we show the GMRT 330 MHz high-resolution contours from Obs No 6153. There are several diffuse sources in the cluster field. The most interesting one, for our purposes, is the central one, which is co-spatial with the core of the cluster, as it is typical for radio mini halos (Mazzotta & Giacintucci 2008; Giacintucci et al. 2014b). The flux density of this source, measured inside the 3-σ contours shown in Fig. 8 (left panel) is ∼12 mJy and its LAS in the east-west direction is ∼80″ corresponding to ∼370 kpc.

On the right panel of Fig. 8 we also show the low-resolution contours of the same portion of the sky (derived from Obs No 6837), where some diffuse emission seems to be present on a larger scale. However, the image has a fairly low sensitivity (rms noise ∼1 mJy beam^{-1} with beam = 57″ × 42″) and the discrete sources in the cluster field (which have not been subtracted out) may largely contribute to the apparently extended emission. We fitted the surface brightness profile of the diffuse source in A402 with the technique discussed in Sect. 6 and we found a central surface brightness $I_0 = 9.1 \pm 1.1$ μJy arcsec^{-2} and an e-folding radius $r_e = 84.8 \pm 13.9$ kpc. These values would place A402 among mini halos in the $I_0 - r_e$ diagram from Murgia et al. (2009). To be cautious we consider the diffuse emission in A402 as a candidate mini halo[6].

4.5. Radio diffuse emission in the full sample

The observational campaign carried out during this work has enabled the completion of the radio information of our sample. In summary, among the 75 clusters presented in Table 1, there are: 28 (∼37%) radio halos, ten of which are USSRHs or candidate USSRHs; seven (∼10%) radio relics, five of which in clusters with radio halos (already counted above); 11 (∼15%) mini halos, two of which show steep spectrum emission on a larger scale; five candidate radio halos and one candidate mini halo (∼8%); 31 (∼41%) clusters without central diffuse emission (two of which host relics, already counted above).

[6] While this paper was in preparation, Giovannini et al. (2020) classified the diffuse emission in A402 as a radio halo, using a short JVLA observation (25 min in C array and 10 min in D array), however the concerns about the possible contamination from the discrete sources apply also in this case.

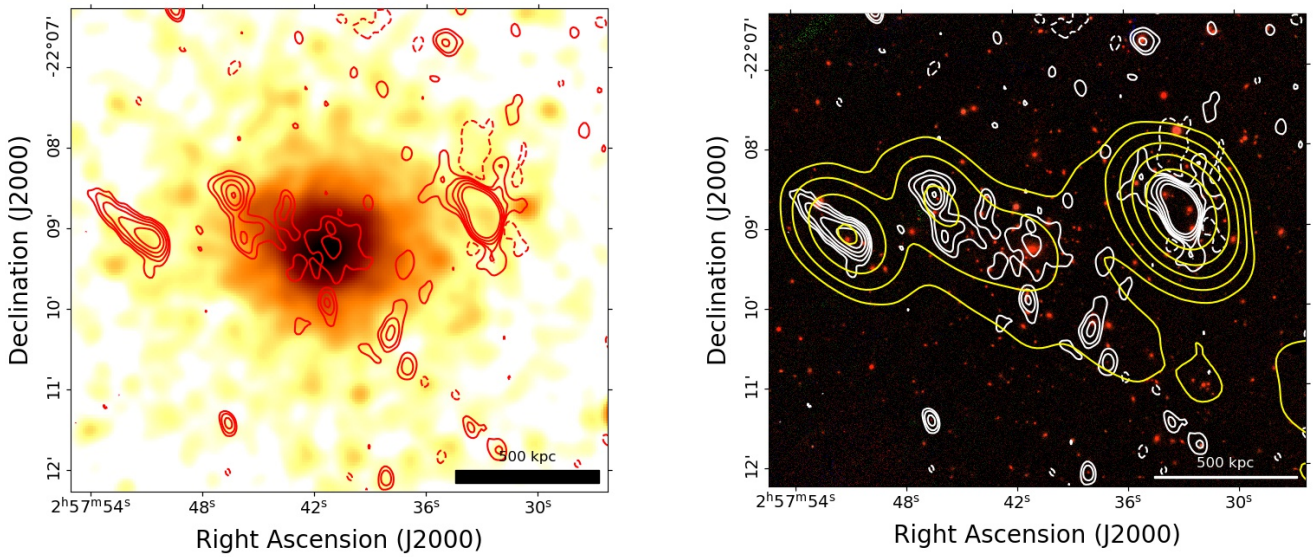

Fig. 8. Images of the cluster A402. *Left*: GMRT 330 MHz contours superimposed on the X-ray *Chandra* image of the cluster. Contours start at 0.35 mJy beam^{-1} and are spaced by a factor of two. The first negative contour is dashed. The beam is 13.4″ × 8.6″ and the rms noise of the radio image is ∼0.1 mJy beam^{-1}. *Right*: PanSTARRS optical image of the field of A402 with the same contours of the left panel (white) plus the low-resolution GMRT 330 MHz contours (yellow). Contours start at 3 mJy beam^{-1} and are spaced by a factor of two. The rms noise of the low-resolution image is ∼1 mJy beam^{-1} with beam = 57″ × 42″.

5. Non-detections and upper limits

Among the 31 clusters of the sample without radio halos, 17 have been analysed in this paper (Table 4). High-resolution images of fields of ∼10′ × 10′ centred on the cluster centre are shown in Appendix A. To extract quantitative information from the non-detection of radio halos in it is crucial to derive meaningful upper limits to the diffuse flux density of those clusters. Due to the bad quality of four of the datasets listed in Table 4, in the following, we will derive upper limits for 13 clusters. The issues related to these four clusters will be briefly discussed at the end of this section. We adopted the method of injecting mock radio halos in the *uv*-datasets. The injection technique was introduced in the GMRT Radio Halo Survey (Brunetti et al. 2007; Venturi et al. 2007, 2008; Kale et al. 2013, 2015) and it has been used in the literature since then (Dallacasa et al. 2009; Russell et al. 2011; Bonafede et al. 2017; Johnston-Hollitt & Pratley 2017; Cuciti et al. 2018).

In this work, following Bonafede et al. (2017), we modelled the radio halo brightness profile with an exponential law in the form:

$$I(r) = I_0 e^{-\frac{r}{r_e}}, \quad (1)$$

where I_0 is the central surface brightness and r_e is the e-folding radius (Orrú et al. 2007; Murgia et al. 2009). In order to inject Megaparsec scale radio halos, as reference we used r_e = 500 kpc/2.6 = 192 kpc, where 2.6 is the median value of the quantity R_H/r_e for the radio halos studied by both Murgia et al. (2009) and Cassano et al. (2007) (Bonafede et al. 2017). In particular, R_H is calculated, in Cassano et al. (2007), as $R_H = \sqrt{R_{\rm min} \times R_{\rm max}}$, where $R_{\rm min}$ and $R_{\rm max}$ are the minimum and maximum radii of the 3-σ surface brightness isocontours.

For each cluster, we chose a region in the image, close to the pointing center and void of sources and clear noise pattern and we created a set of mock radio halos with different integrated flux densities, centred on that region. We added the modelled radio halos to the datasets and, for each modified dataset, we followed the same procedures described in the previous sections to produce images optimised for the detection of the extended emission. For a given cluster mass, we started injecting a mock radio halo that would lie on the radio power–mass correlation from Cassano et al. (2013) and we reduced the injected flux density until the injected radio halo appeared just as some positive residuals leading to the 'suspect' of diffuse emission. More quantitatively, we stop when the largest linear scale (2-σ contours) of the recovered halo is ∼2 × r_e, implying that only ∼30% of the injected flux has been recovered, in line with the approach used in Bonafede et al. (2017) and Cuciti et al. (2018). The injected flux density corresponding to this marginal detection can be considered as the upper limit for that particular cluster. We did not inject the mock radio halo at the cluster centre because the possible presence of some weak residual emission in the cluster field may favour the detection of the mock radio halo, biasing our upper limit towards lower values. Furthermore, faint cluster radio galaxies below the detection limit of our observations may contribute to a positive plateau in the cluster field (e.g. Farnsworth et al. 2013; Cuciti et al. 2015). An example of the injection procedure is shown in Fig. 9 for the cluster A220: the original image is in the upper left panel and a series of fake radio halos with decreasing flux densities is in the other panels. As a sanity check, we fitted the surface brightness radial profile, with the technique described in Sect. 6, of an injected mock halo. In particular, we focused on A2104 and we injected a mock halo with flux density 70 mJy and r_e = 150 kpc (I_0 = 4.3 μJy arcsec^{-2}). We obtained r_e = 147 ± 15 kpc and I_0 = 3.4 ± 0.4 μJy arcsec^{-2} as best fit parameters. We repeated this test with flux densities in the range 50–70 mJy and r_e in the range 100–192 kpc, obtaining a discrepancy of ∼15% at most with respect to the injected values.

We applied this procedure to the 17 clusters listed in Table 4. We scaled the upper limit to 1.4 GHz, assuming a spectral index α = −1.3, for clusters with GMRT 330 or 610 MHz data only (Table 4). In general, the possibility to place deep upper limits is related to the quality of the images in terms of sensitivity, density of the inner *uv*-coverage and presence of bright sources with residual calibration errors. In line with the results

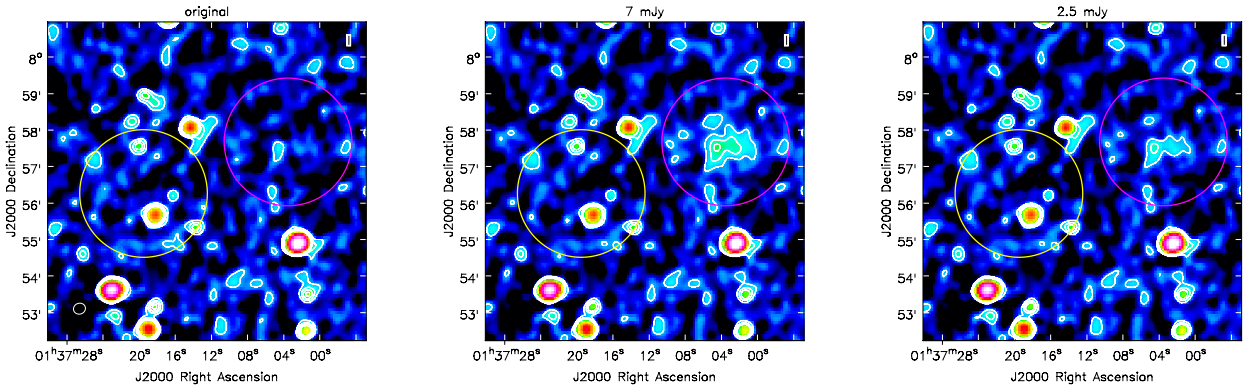

Fig. 9. Injection of mock radio halos in the cluster A220. *Left*: original image. *Middle*: injected radio halo with flux density of 7 mJy. *Right*: injected radio halo with flux density of 2.5 mJy. Contours start at 2-σ rms noise. The two circles have radii of $2.6 \times r_e = 500$ kpc and are centred on the cluster centre (yellow) and on the modelled radio halo (magenta). We consider 2.5 mJy to be the upper limit to the diffuse emission of A220.

from Venturi et al. (2008), we found that the presence of radio halos with flux densities $\gtrsim$10 mJy can be safely established with GMRT 610 MHz observations, while injected radio halos of 5–10 mJy appear in the images as positive residuals that would lead to the suspect of diffuse emission and can be thus considered as upper limits. The values of the upper limits obtained with the JVLA range from 2 to 5 mJy.

Unfortunately, we were not able to derive reliable upper limits for four clusters: RXC J0510.7–0801, RXC J1322.8+3138, A1437 and Zwcl1028.8+1419. The GMRT 610 MHz and 240 MHz images of RXC J0510.7–0801 are affected by the presence of a strong radio source in the field, whose sidelobes cross the cluster field even after several runs of self-calibration and peeling (Kale et al. 2015, see also Fig. A.15). The field of RXC J1322.8+3138 is dominated by an FRII radio galaxy extending over $\sim$11.5′ close to the cluster region (Fig. A.11). This source limited the possibility of producing sensitive low-resolution images. A lot of editing was needed for the datasets of A1437 and Zwcl1028.8+1419, especially at the short baselines; this, combined with the relatively high noise level of the images, did not allow a useful upper limit to be derived. We observed Zwcl1028.8+1419 with LOFAR and RXC J1322.8+3138 has been observed with LOFAR as part of LoTSS. We carried out a preliminary analysis of these observations and we anticipate that they do not suggest the presence of clear diffuse emission on the cluster scale.

6. Surface brightness radial profile

Following the approach described in Murgia et al. (2009), we derived the azimuthally averaged surface brightness radial profile for the confirmed radio halos in our sample, and we fitted them with an exponential law in the form (1) in order to derive the central surface brightness, I_0, and the e-folding radius, r_e. To do that, we used low-resolution source-subtracted images, convolved with a Gaussian circular beam. In case the image contains diffuse sources that cannot be properly subtracted we masked them (see e.g. the case of A2744 in Fig. B.5, where the radio relic has been masked) and we did not consider the masked pixels when calculating the surface brightness. We averaged the radio brightness in concentric annuli, centred on the peak of the image (Fig. 10, right panel). The width of the annuli was chosen to be half of the FWHM of the beam of the image. We considered only annuli with an average surface brightness profile higher than two times the rms noise of the image. We note that the estimated fitting parameters differs only marginally (<5%) if we consider only annuli with an average surface brightness profile higher than three times the rms noise of the image. We first generated a two–dimensional model using Eq. (1) with the same size and pixel size of the radio image and we convolved it with a Gaussian with the FWHM equal to the beam of the image. Then, we azimuthally averaged the exponential model with the same set of annuli used for the radio halo. The one-dimensional surface brightness profile of the two-dimensional exponential model (convolved with the beam) is our fitting model (see e.g. the black line in Fig. 10), which takes into account the resolution of the image and the uncertainties associated with the sampling of the radial profile. We show the radial profile of the radio halo in A2163 with the best fit model in Fig. 10, the others are shown in Appendix B.

This method is based on the assumption that radio halos have a central peak and then the brightness decreases with increasing distance from the centre. This assumption is valid for most of the radio halos in our sample, however, ten radio halos (Z0104, R2003, A520 and A1351, A3411, R1514, A1300, A1132, A2142, A1443) clearly have multiple peaks, We did not include these radio halos in the analysis of the radial profiles. Moreover, we excluded four radio halos for which we do not have suitable source subtracted images (A1451, A3888, A2261, A1689). Thus, we derived and fitted the radial surface brightness profile of the 14 radio halos listed in Table 3. These radial profiles, together with the set of annuli used to derive them and the best fit model are shown in Appendix B. In Table 3 we summarise the best fit parameters, I_0 and r_e and the reduced χ^2 of the fit. We will use this information to derive the emissivity of radio halos in Paper II.

7. X-ray data analysis

In this Section we describe the analysis of the dynamical properties of the clusters of our sample. Among the 75 clusters of the sample, 63 have archival X-ray *Chandra* data. 54 of them already have literature information on their dynamical status (Cassano et al. 2010, 2013, 2016; Cuciti et al. 2015). We produced and analysed the *Chandra* images of the remaining nine clusters (marked with $\surd$ in Table 5). *Chandra* X-ray data were processed with CIAO 4.5 using calibration files from CALDB 4.5.8. Standard techniques to correct time-dependent issues were applied[7], the screening of the events file was applied to filter out

[7] http://cxc.harvard.edu/ciao/threads/index.html

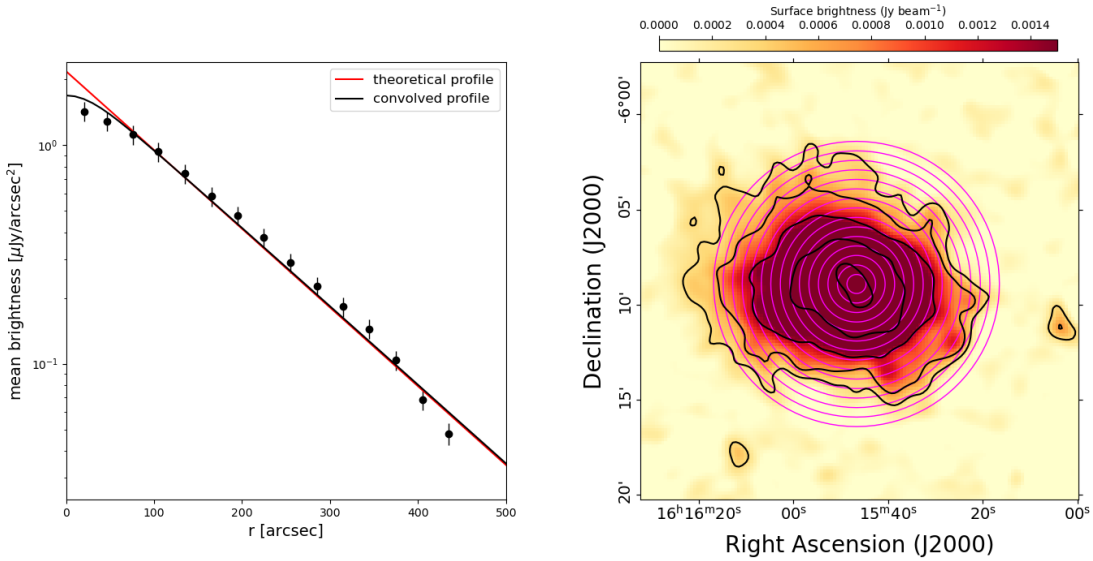

Fig. 10. Radial surface brightness profile of the radio halo in A2163. *Left*: data points represents the averaged surface brightness measured in the annuli shown in the right panel. The red curve is the theoretical exponential profile, the black curve is the profile convolved with the beam of the image. *Right*: VLA 1.4 GHz image from where the profile on the left panel has been extracted. The magenta annuli represent the regions where the average surface brightness was measured. Contours start at 3−σ and are spaced by a factor of two. The 1-σ rms noise of the image is 0.1 mJy beam^{-1} with beam = 60″ × 60″.

strong background flares, cosmic rays and soft protons. We identified point sources with an automatic algorithm and we removed them from the images. Images were normalised for the exposure map of the observation.

Following Cassano et al. (2010, 2013) and Cuciti et al. (2015), we produced *Chandra* images in the 0.5–2 keV band and we analysed the X-ray surface brightness inside an aperture radius R_{ap} = 500 kpc, centred on the cluster X-ray peak. 500 kpc is the typical radius of radio halos, in this way we evaluate the morphological properties of clusters within the region where energy is most likely dissipated and generates synchrotron emission. To provide a quantitative measure of the level of dynamical disturbance of the clusters, we used three methods, widely used in the literature to investigate the dynamics of cluster: the power ratios, P_3/P_0 (e.g. Buote & Tsai 1995; Jeltema et al. 2005; Ventimiglia et al. 2008; Böhringer et al. 2010; Cassano et al. 2016; Lovisari et al. 2017), the centroid shift, w (e.g. Mohr et al. 1993; Poole et al. 2006; O'Hara et al. 2006; Ventimiglia et al. 2008; Maughan et al. 2008; Böhringer et al. 2010; Cassano et al. 2016; Lovisari et al. 2017) and the concentration parameter, c (e.g. Santos et al. 2008; Parekh et al. 2015; Cassano et al. 2016; Rossetti et al. 2017). The power ratios represent the multipole decomposition of the mass distribution within the aperture radius. We only used the third moment, P_3/P_0, which is sensitive to the presence of substructures indicating ongoing dynamical activity (Böhringer et al. 2010). The centroid shift, w, is defined as the standard deviation of the projected separation between peak and the centroid of the X-ray emission. The concentration parameter is the ratio between the surface brightness inside the central region (100 kpc radius) and the 'ambient' surface brightness (inside a radius of 500 kpc).

We refer to Cassano et al. (2010) (and references therein), for a detailed description of the morphological parameters. Here we just mention that, in general, relaxed clusters have high values of c and low values of w and P_3/P_0. Conversely, dynamically disturbed clusters have low values of c and high values of w and P_3/P_0.

Table 3. Radio halo brightness profiles.

Name	r_e (kpc)	I_0 (μJy/arcsec^2)	χ^2
A773	203 ± 14	0.42± 0.05	0.16
A665	209 ± 14	0.89 ± 0.08	1.10
A209	225 ± 10	0.58 ± 0.05	1.88
A2163	402 ± 10	2.18 ± 0.11	1.16
A2218	82 ± 5	1.27 ± 0.15	1.97
A2744	261 ± 8	3.02 ± 0.02	0.55
Z0634	116 ± 14	0.70 ± 0.10	2.14
A2219	246 ± 12	1.31 ± 0.10	0.41
A1758	191 ± 13	1.71 ± 0.18	3.26
A697	184 ± 7	4.24 ± 0.34	8.02
RXC J1314.4–2515	60 ± 4	7.45 ± 0.89	1.43
A521	187 ± 6	8.49 ± 0.57	2.21
PSZ1 G171.96-40.64	253 ± 15	1.35 ± 0.11	2.23
RXC J0142.0+2131	147 ± 18	4.74 ± 0.63	0.49

8. Dynamical properties

In this section we characterise the dynamical properties of the clusters of our sample on the basis of their X-ray emission. The distributions of the morphological parameters are shown in Fig. 11, both for all the clusters (black) and for two mass bins containing the same number of objects (the mass separating the two bins is $M_{500} = 7 \times 10^{14}\ M_\odot$). We do not find a significant dependence of the morphological parameters on the cluster mass, in line with other recent results (Rossetti et al. 2017; Lovisari et al. 2017).

The most efficient way to characterise the dynamical properties of clusters is the combination of two morphological parameters, at least. In this Section we focus on the combination between c and w, which has been shown to be a robust approach to distinguish between merger and relaxed clusters

Table 4. Clusters without detected extended emission.

Cluster name	rms (mJy/beam)	Beam ($''\times''$)	UL $^{(*)}$ (mJy)	$P_{1.4\,\mathrm{GHz}}$ $^{(**)}$ (10^{23} W Hz^{-1})
JVLA *L*-band				
A56$^{(C)}$	0.09	19.8×19.2	4	12
A2813$^{(C)}$	0.055	20.5×18.1	5	14
A2895$^{(C)}$	0.055	22.4×17.9	3	5
A220$^{(C)}$	0.055	27.6×26.3	2.5	9.7
A384$^{(C)}$	0.045	28.3×26.0	4	7.4
A2472$^{(C)}$	0.06	18.1×17.4	3	10
A2355$^{(C)}$	0.08	28.2×24.2	5	8.3
RXC J2051.1+0216$^{(C)}$	0.04	19.8×18.3	2	7.3
RXC J0616.3–2156$^{(D)}$	0.08	78.3×52.8	3	2.5
GMRT 610 MHz				
Zwcl1028.8+1419	0.25	18.6×16.0	–	–
RXC J1322.8+3138	0.35	19.2×17.8	–	–
A1733	0.34	34.7×27.0	7	5.3
PSZ1 G019.12+3123	0.08	21.5×18.0	7	6.3
MACS J2135–010	0.2	21.6×17.2	10	11.7
RXC J0510.7–0801	0.2	5.4×4.8	–	–
GMRT 330 MHz				
A1437	0.27	19.4×16.5	–	–
A2104	0.25	20.6×19.6	25	2.4

Notes. Top panel: upper limits (UL) derived with JVLA *L*-band (C) C array or (D) D array observations. Middle panel: UL derived with GMRT 610 MHz observations. Bottom panel: UL derived with GMRT 330 MHz observations. $^{(*)}$Flux density of the UL measured at the observing frequency. $^{(**)}$Radio power of the UL at 1.4 GHz. For UL derived at 330 or 610 MHz we assumed a spectral index $\alpha = -1.3$.

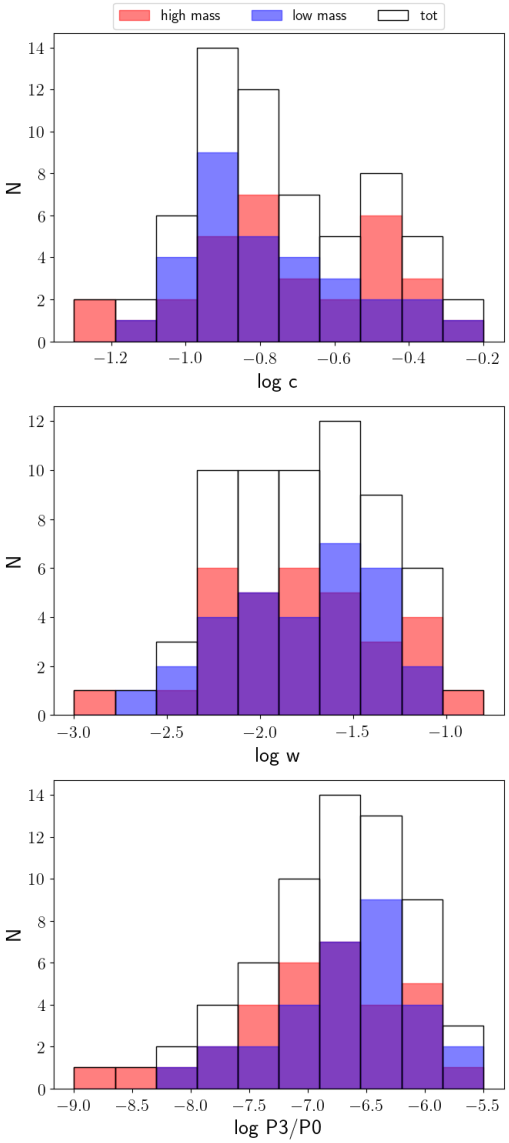

Fig. 11. Concentration parameter (*top*), centroid shift (*middle*) and power ratios (*bottom*) distribution of the clusters with available X-ray *Chandra* data. The red histogram refers to high mass clusters($M_{500} \geq 7\times10^{14}\,M_{\odot}$), while the blue histogram refers to low mass ($M_{500} < 7\times10^{14}\,M_{\odot}$) clusters.

(Lovisari et al. 2017). Figure 12 shows the distribution of the 63 clusters of our sample with available X-ray *Chandra* data in the $c-w$ morphological diagram. As expected, c and w are anti-correlated and the level of dynamical disturbance increases going from the top left to the bottom right corner of the diagram.

Defining a meaningful threshold between relaxed and merging clusters in the $c-w$ morphological diagram is not trivial since projection effects also play a role, in particular for unrelaxed clusters. Lovisari et al. (2017) has recently established the dynamical status of 150 galaxy clusters from the ESZ *Planck* catalogue (Planck Collaboration X 2011) by visually inspecting their *XMM-Newton* images. The results of the visual inspection have been then combined with a number of morphological parameters, including c, w and P_3/P_0, to determine the threshold values between merging and relaxed clusters. They found that among the clusters with a clear dynamical classification (excluding 'intermediate' cases) ~40% are relaxed and ~60% are merging. Similar fractions have been obtained for mass-selected samples using cool core versus non-cool core clusters as indication of relaxed systems and non relaxed systems (Rossetti et al. 2017; Andrade-Santos et al. 2017). Unfortunately, we cannot simply adopt the threshold found in Lovisari et al. (2017) because the parameters are measured within different apertures. Still, we note that the classification of merging and relaxed clusters based on the lines derived by Cassano et al. (2010) to separate radio halo and non-radio halo clusters provides similar results. Indeed ~40% of our clusters lie on the upper left panel of Fig. 12. This suggests that, although those lines were not derived to distinguish merging from relaxed clusters, they still give reasonable statistical information on the dynamical status of the clusters. Such classification of all the clusters of our sample, based on these lines is reported in Table 5.

In addition, following Lovisari et al. (2017), we visually classified each cluster on the basis of the X-ray *Chandra* image (Table 5, Col. 6). In particular, we identified three classes of clusters marked with '*M*', 'int' or '*R*' in Table 5. '*M*' represents clusters where the distribution of the X-ray surface brightness and the presence of pronounced substructures clearly indicates merging activity, '*R*' represents relaxed clusters with circular X-ray morphology and peaked cores, while 'int' indicates intermediate cases, where the morphology is fairly regular, sometimes with a peaked core, but with substructures or features in the X-ray distribution indicating a more complex situation. The two methods of classification are consistent for clusters lying at the opposite corners of the $c-w$ morphological diagram. Although the visual classification is subjective, we noted that, among fairly relaxed clusters, there are some systems showing minor disturbances that may not be caught by morphological parameters. These might be minor mergers, to which the cool core survives,

Table 5. Dynamical properties of clusters.

Name	c	w (10^{-2})	P3/P0 (10^{-7})	Dynamics	Visual inspection
A2163	0.116	5.970	14.850	$M^{(1)}$	M
A2219	0.134	2.127	1.681	$M^{(1)}$	M
A2744	0.101	2.637	10.500	$M^{(1)}$	M
A1758a	0.109	8.217	2.515	$M^{(1)}$	M
RXCJ2003.5–2323	0.062	1.824	4.602	$M^{(1)}$	M
A1300	0.191	4.442	6.847	$M^{(1)}$	M
A773	0.184	2.403	1.445	$M^{(1)}$	M
A209	0.176	1.321	0.518	$M^{(1)}$	M
A520	0.097	10.050	5.259	$M^{(1)}$	M
A521	0.108	2.204	5.090	$M^{(1)}$	M
A697	0.153	0.731	1.668	$M^{(1)}$	M
A1351	0.083	4.272	3.506	$M\surd$	M
A665	0.164	5.826	6.311	$M\surd$	M
A1689	0.363	0.463	0.076	$R\surd$	$M*$
A1914	0.221	5.432	1.646	$M\surd$	M
A2142	0.234	1.451	0.674	$R\surd$	int
A2218	0.184	0.858	0.474	$M\surd$	int
A1443	0.108	3.530	12.890	$M\surd$	M
A3411	0.092	1.949	2.647	$M\surd$	M
RXC J1514.9–1523	0.064	1.301	1.411	$M\surd$	M
A2390	0.304	1.171	0.694	$R^{(1)}$	int
A1132	0.111	3.386	3.059	$M\surd$	M
Zwcl 0634.1+4750	0.139	0.988	5.375	$M\surd$	M
Zwcl 0104.9+5350	0.088	5.693	0.604	$M\surd$	M
A3888	0.163	2.447	0.877	$M\surd$	M
A2261	0.334	0.494	1.026	$R^{(1)}$	int
PSZ1 G171.96-40.64	0.144	2.318	1.086	$M\surd$	M
PSZ1 G139.61+24.20	0.362	1.348	0.193	$R\surd$	int
RXC J1504.1–0248	0.624	0.459	0.147	$R^{(1)}$	R
A1835	0.486	0.996	0.458	$R\surd$	R
A478	0.328	0.529	0.012	$R\surd$	R
A1413	0.265	0.183	0.084	$R\surd$	int
S780	0.473	0.827	0.480	$R^{(1)}$	R
A2204	0.537	0.125	0.022	$R\surd$	R
RXJ1720.1+2638	0.489	0.279	0.117	$R\surd$	R
A3444	0.465	0.745	0.433	$R\surd$	R
A2667	0.406	0.926	1.395	$R^{(1)}$	int
A402	0.323	1.249	1.350	$R\surd$	R
A2104	0.123	2.198	2.082	$M\surd$	M
A1733	0.133	4.219	2.674	$M\surd$	M
A2355	0.075	4.879	7.495	$M\surd$	M
A2631	0.121	1.574	1.550	$M^{(1)}$	M
A781	0.111	6.374	3.143	$M^{(1)}$	M
RXC J0142.0+2131	0.186	0.738	6.625	$M^{(2)}$	int
A1423	0.331	0.562	1.413	$R^{(1)}$	M
A2537	0.278	0.561	0.351	$R^{(1)}$	M
A3088	0.339	0.284	0.833	$R^{(2)}$	R
A1576	0.235	1.271	5.950	$R^{(2)}$	M
A1763	0.139	1.885	1.222	$M\surd$	M
A68	0.149	1.004	3.199	$M\surd$	M
A1437	0.085	7.450	9.505	$M\surd$	M
RXC J0616.3–2156	0.115	3.042	0.614	$M\surd$	M
A2895	0.161	4.271	4.851	$M\surd$	M
RXC J0510.7–0801	0.134	2.346	2.171	$M\surd$	M
MACS J2135-010	0.138	1.188	4.073	$M\surd$	M
A2813	0.172	0.311	1.230	$R\surd$	int
A115	0.236	6.305	13.140	$M\surd$	M
A2345	0.112	3.932	19.090	$M\surd$	M
A2552	0.218	0.639	0.222	$R\surd$	M
Zwcl 2120.1+2256	0.197	1.189	3.961	$M\surd$	int
Z5247	0.158	3.362	3.061	$M\surd$	M
A1682	0.126	2.054	15.320	$M^{(1)}$	M
A3041	0.099	3.342	13.620	$M\surd$	M
A56	–	–	–	–	M
A2697	–	–	–	–	R
RXC J1314.4–2515	–	–	–	–	M
A1451	–	–	–	–	M
RXC J2051.1+0216	–	–	–	–	M
RXC J1322.8+3138	–	–	–	–	int
A384	–	–	–	–	R
PSZ1 G019.12+3123	–	–	–	–	int
A2472	–	–	–	–	int
PSZ1 G205.07-6294	–	–	–	–	M

Notes. Upper panel: clusters with available X-ray *Chandra* data. Lower panel: clusters with available *XMM-Newton* data.
References. $\surd$ This work; [(1)] Cassano et al. (2010); [(2)] Cassano et al. (2013); [(3)] Cassano et al. (2016); [(4)] Cuciti et al. (2015); [(5)] Bonafede et al. (2015) * based on optical studies performed by Andersson & Madejski (2004).

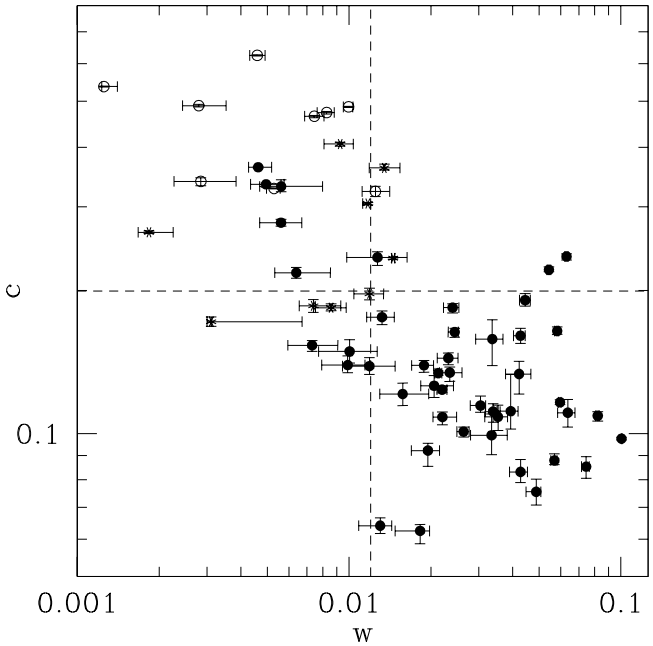

Fig. 12. $c - w$ morphological diagram. Filled dots are clusters classified as merging from the visual inspection, empty dots are visually classified as relaxed and asterisks are visually classified as intermediate. Black lines are adapted from Cassano et al. (2010) and are $c = 0.2$ and $w = 0.012$.

but the X-ray distribution shows edges or irregularities. Alternatively, there may be signatures of disturbance on larger scales with respect to the radius adopted to measure the parameters, such as sub-clumps in the cluster outskirts.

Among the 12 clusters of our sample without available *Chandra* data, ten have archival *XMM-Newton* data. We did not derive morphological parameters for the clusters observed only with *XMM-Newton*, to avoid introducing biases due to the different PSF and effective area compared to *Chandra*. We classified the dynamical status of these clusters by visually inspecting their *XMM-Newton* images and we report these classifications in the bottom panel of Table 5. We could not infer the dynamical status of the two clusters without pointed X-ray observations.

9. The full sample: Summary and conclusions

In this paper we built the largest mass-selected sample of galaxy clusters with deep radio observations available to date. It is made of 75 clusters with $z = 0.08-0.33$ and $M_{500} \gtrsim 6 \times 10^{14}\,M_{\odot}$ selected from the *Planck* SZ catalogue (Planck Collaboration XXIX 2014). Thanks to the radio data analysis described in Sects. 3, now each cluster of the sample has at least one pointed observation from which we have information about the possible presence of radio diffuse emission.

Beyond the statistical value of this work, the large amount of radio data analysed led to the discovery of new radio halos, mini halos and candidate diffuse sources in clusters (Sect. 4). In particular, A1451 and Z0634 host radio halos (Cuciti et al. 2018) and PSZG139 host a mini halo surrounded by steep spectrum large scale emission (Savini et al. 2018). We found candidate radio halos in Z2120, A3041 and a conservatively claimed a candidate mini halo in A402. Furthermore, we followed up the known radio halos in A3888 and A1443 at different frequencies.

For clusters without any hint of diffuse emission in our observations we used the injection technique to derive upper limits to their diffuse flux (Sect. 5).

The great majority of the clusters of this sample have X-ray *Chandra* data. We analysed those data to derive information about the dynamical state of clusters (Sect. 7). According to the morphological classification based on the combination of centroid shift and concentration parameter, ∼40% of the clusters of our sample are relaxed and ∼60% are merging, in line with other recent results (Lovisari et al. 2017; Rossetti et al. 2017; Andrade-Santos et al. 2017). In addition, we visually inspected all the *Chandra* images and the *XMM-Newton* images of clusters without *Chandra* data to give an independent classification of the dynamical status of clusters.

The properties (coordinates, redshift, M_{500}, R_{500}, radio classification and radio power at 1.4 GHz) of the clusters of the sample are listed in Table 1. Radio powers in Table 1 are calculated at 1.4 GHz and are k-corrected. When α is unknown, we assume $\alpha = -1.3$.

We summarise below the diffuse sources present in our sample (references are given in Table 1):

- 28 (∼37%) clusters host radio halos, ten of which are USSRHs or candidate USSRHs
- seven (∼10%) clusters have radio relics, five of which also have radio halos (and have been also counted among radio halos above), and two of which are without radio halos
- 11 (∼15%) clusters have mini halos
- 31 (∼41%) clusters do not show any hint of central diffuse emission at the sensitivity of current observations[8].

Moreover, we found candidate diffuse emission in six clusters, one is a candidate mini halo and five are candidate radio halos. Combining our results (Sect. 5) with the work done by Venturi et al. (2008), and Kale et al. (2013, 2015) for the GMRT Radio Halo Survey and Bonafede et al. (2017) we have upper limits for 22 clusters. Being obtained with similar techniques (Sect. 5), the upper limits from the literature are comparable with those derived in this work. The statistical analysis of the properties of radio halos in this sample, including the radio power-mass diagram, the radio emissivity-mass diagram, the radio halo-merger connection, and the occurrence of radio halos will be presented in Paper II.

[8] The two cluster with radio relics but without radio halos (A115 and A2345) are among these 31 clusters.

Acknowledgements. The authors thank the anonymous referee for the comments that improved the presentation of the paper. VC acknowledges support from the Alexander von Humboldt Foundation. AB acknowledges support from the ERC through the grant ERC-Stg Dranoel n. 714245 and from the MIUR FARE grant SMS. RJvW acknowledges support from the VIDI research programme with project number 639.042.729, which is financed by the Netherlands Organisation for Scientific Research (NWO). RK acknowledges the support of the Department of Atomic Energy, Government of India, under project no. 12-R&D-TFR-5.02-0700. Basic research in radio astronomy at the Naval Research Laboratory is supported by 6.1 Base funding. SE acknowledges financial contribution from the contracts ASI-INAF Athena 2019-27-HH.0, "Attività di Studio per la comunità scientifica di Astrofisica delle Alte Energie e Fisica Astroparticellare" (Accordo Attuativo ASI-INAF n. 2017-14-H.0), INAF mainstream project 1.05.01.86.10, and from the European Union's Horizon 2020 Programme under the AHEAD2020 project (grant agreement n. 871158). GWP acknowledges the support of the French space agency, CNES. The National Radio Astronomy Observatory is a facility of the National Science Foundation operated under cooperative agreement by Associated Universities, Inc. We thank the staff of the GMRT that made these observations possible. GMRT is run by the National Centre for Radio Astrophysics of the Tata Institute of Fundamental Research. The scientific results reported in this article are based in part on data obtained from the *Chandra* Data Archive. This research has made use of the NASA/IPAC Extragalactic Database (NED) which is operated by the Jet Propulsion Laboratory, California Institute of Technology, under contract with the National Aeronautics and Space Administration.

References

Andernach, H., Sievers, A., Kus, A., & Schnaubelt, J. 1986, A&AS, 65, 561
Andersson, K. E., & Madejski, G. M. 2004, ApJ, 607, 190
Andrade-Santos, F., Jones, C., Forman, W. R., et al. 2017, ApJ, 843, 76
Bacchi, M., Feretti, L., Giovannini, G., & Govoni, F. 2003, A&A, 400, 465
Basu, K. 2012, MNRAS, 421, L112
Böhringer, H., Pratt, G. W., Arnaud, M., et al. 2010, A&A, 514, A32
Bonafede, A., Intema, H., Brüggen, M., et al. 2015, MNRAS, 454, 3391
Bonafede, A., Cassano, R., Brüggen, M., et al. 2017, MNRAS, 470, 3465
Botteon, A., Shimwell, T. W., Bonafede, A., et al. 2018, MNRAS, 478, 885
Briggs, D. S. 1995, Am. Astron. Soc. Meeting Abstracts, 187, 112.02
Brunetti, G., & Jones, T. W. 2014, Int. J. Mod. Phys. D, 23, 1430007
Brunetti, G., & Lazarian, A. 2007, MNRAS, 378, 245
Brunetti, G., & Lazarian, A. 2011, MNRAS, 410, 127
Brunetti, G., & Lazarian, A. 2016, MNRAS, 458, 2584
Brunetti, G., Setti, G., Feretti, L., & Giovannini, G. 2001, MNRAS, 320, 365
Brunetti, G., Venturi, T., Dallacasa, D., et al. 2007, ApJ, 670, L5
Brunetti, G., Giacintucci, S., Cassano, R., et al. 2008, Nature, 455, 944
Brunetti, G., Cassano, R., Dolag, K., & Setti, G. 2009, A&A, 507, 661
Buote, D. A., & Tsai, J. C. 1995, ApJ, 452, 522
Cassano, R., Brunetti, G., Setti, G., Govoni, F., & Dolag, K. 2007, MNRAS, 378, 1565
Cassano, R., Ettori, S., Giacintucci, S., et al. 2010, ApJ, 721, L82
Cassano, R., Ettori, S., Brunetti, G., et al. 2013, ApJ, 777, 141
Cassano, R., Brunetti, G., Giocoli, C., & Ettori, S. 2016, A&A, 593, A81
Cavagnolo, K. W., Donahue, M., Voit, G. M., & Sun, M. 2008, ApJ, 682, 821
Cavagnolo, K. W., Donahue, M., Voit, G. M., & Sun, M. 2009, ApJS, 182, 12
Chandra, P., Ray, A., & Bhatnagar, S. 2004, ApJ, 612, 974
Chon, G., Böhringer, H., & Smith, G. P. 2012, A&A, 548, A59
Colless, M., Peterson, B. A., Jackson, C., et al. 2003, ArXiv e-prints [arXiv:astro-ph/0306581]
Condon, J. J., Cotton, W. D., Greisen, E. W., et al. 1998, AJ, 115, 1693
Cornwell, T. J., Golap, K., & Bhatnagar, S. 2005, in Astronomical Data Analysis Software and Systems XIV, eds. P. Shopbell, M. Britton, & R. Ebert, ASP Conf. Ser., 347, 86
Cornwell, T. J., Golap, K., & Bhatnagar, S. 2008, IEEE J. Sel. Top. Signal Process., 2, 647
Cuciti, V., Cassano, R., Brunetti, G., et al. 2015, A&A, 580, A97
Cuciti, V., Brunetti, G., van Weeren, R., et al. 2018, A&A, 609, A61
Cuciti, V., Cassano, R., Brunetti, G., et al. 2021, A&A, 647, A51
Dallacasa, D., Brunetti, G., Giacintucci, S., et al. 2009, ApJ, 699, 1288
Ensslin, T. A., Biermann, P. L., Klein, U., & Kohle, S. 1998, A&A, 332, 395
Farnsworth, D., Rudnick, L., Brown, S., & Brunetti, G. 2013, ApJ, 779, 189
Feretti, L., Fusco-Femiano, R., Giovannini, G., & Govoni, F. 2001, A&A, 373, 106
Giacintucci, S., & Venturi, T. 2009, A&A, 505, 55
Giacintucci, S., Venturi, T., Macario, G., et al. 2008, A&A, 486, 347
Giacintucci, S., Markevitch, M., Brunetti, G., Cassano, R., & Venturi, T. 2011a, A&A, 525, L10

Giacintucci, S., Dallacasa, D., Venturi, T., et al. 2011b, A&A, 534, A57
Giacintucci, S., Kale, R., Wik, D. R., Venturi, T., & Markevitch, M. 2013, ApJ, 766, 18
Giacintucci, S., Markevitch, M., Brunetti, G., et al. 2014a, ApJ, 795, 73
Giacintucci, S., Markevitch, M., Venturi, T., et al. 2014b, ApJ, 781, 9
Giacintucci, S., Markevitch, M., Cassano, R., et al. 2017, ApJ, 841, 71
Giacintucci, S., Markevitch, M., Cassano, R., et al. 2019, ApJ, 880, 70
Giovannini, G., & Feretti, L. 2000, New A, 5, 335
Giovannini, G., Tordi, M., & Feretti, L. 1999, New A, 4, 141
Giovannini, G., Feretti, L., Govoni, F., Murgia, M., & Pizzo, R. 2006, Astron. Nachr., 327, 563
Giovannini, G., Cau, M., Bonafede, A., et al. 2020, A&A, 640, A108
Gitti, M., Brunetti, G., & Setti, G. 2002, A&A, 386, 456
Govoni, F., Feretti, L., Giovannini, G., et al. 2001, A&A, 376, 803
Govoni, F., Murgia, M., Markevitch, M., et al. 2009, A&A, 499, 371
Haarsma, D. B., Leisman, L., Donahue, M., et al. 2010, ApJ, 713, 1037
Hanisch, R. J. 1982, A&A, 111, 97
Intema, H. T. 2014, Astrophysics Source Code Library [record ascl: 1408.006]
Intema, H. T., van der Tol, S., Cotton, W. D., et al. 2009, A&A, 501, 1185
Intema, H. T., Jagannathan, P., Mooley, K. P., & Frail, D. A. 2017, A&A, 598, A78
Jacob, S., & Pfrommer, C. 2017, MNRAS, 467, 1478
Jeltema, T. E., Canizares, C. R., Bautz, M. W., & Buote, D. A. 2005, ApJ, 624, 606
Johnston-Hollitt, M., & Pratley, L. 2017, ArXiv e-prints [arXiv:1706.04930]
Kale, R., Venturi, T., Giacintucci, S., et al. 2013, A&A, 557, A99
Kale, R., Venturi, T., Giacintucci, S., et al. 2015, A&A, 579, A92
Kang, H., Ryu, D., & Jones, T. W. 2012, ApJ, 756, 97
Kempner, J. C., & Sarazin, C. L. 2001, ApJ, 548, 639
Knowles, K., Baker, A., Basu, K., et al. 2016, Proc. MeerKAT Science: On the Pathway to the SKA, 25-27 May, 2016 Stellenbosch, South Africa (MeerKAT2016). Online at https://pos.sissa.it/cgi-bin/reader/conf.cgi?confid=277, 30
Knowles, K., Baker, A. J., Bond, J. R., et al. 2019, MNRAS, 486, 1332
Liang, H., Hunstead, R. W., Birkinshaw, M., & Andreani, P. 2000, ApJ, 544, 686
Lovisari, L., Forman, W. R., Jones, C., et al. 2017, ApJ, 846, 51
Macario, G., Venturi, T., Brunetti, G., et al. 2010, A&A, 517, A43
Mandal, S., Intema, H. T., Shimwell, T. W., et al. 2019, A&A, 622, A22
Markevitch, M., Govoni, F., Brunetti, G., & Jerius, D. 2005, ApJ, 627, 733
Maughan, B. J., Jones, L. R., Pierre, M., et al. 2008, MNRAS, 387, 998
Mazzotta, P., & Giacintucci, S. 2008, ApJ, 675, L9
Mohan, N., & Rafferty, D. 2015, Astrophysics Source Code Library [record ascl:1502.007]
Mohr, J. J., Fabricant, D. G., & Geller, M. J. 1993, ApJ, 413, 492
Motl, P. M., Hallman, E. J., Burns, J. O., & Norman, M. L. 2005, ApJ, 623, L63
Murgia, M., Govoni, F., Markevitch, M., et al. 2009, A&A, 499, 679
Nagai, D. 2006, ApJ, 650, 538
O'Hara, T. B., Mohr, J. J., Bialek, J. J., & Evrard, A. E. 2006, ApJ, 639, 64
Orrú, E., Murgia, M., Feretti, L., et al. 2007, A&A, 467, 943
Parekh, V., van der Heyden, K., Ferrari, C., Angus, G., & Holwerda, B. 2015, A&A, 575, A127
Perley, R. A., & Butler, B. J. 2013, ApJS, 204, 19
Petrosian, V. 2001, ApJ, 557, 560
Pfrommer, C., & Enßlin, T. A. 2004, A&A, 413, 17
Pinzke, A., Oh, S. P., & Pfrommer, C. 2013, MNRAS, 435, 1061
Pinzke, A., Oh, S. P., & Pfrommer, C. 2017, MNRAS, 465, 4800
Planck Collaboration X. 2011, A&A, 536, A10
Planck Collaboration XXIX. 2014, A&A, 571, A29
Poole, G. B., Fardal, M. A., Babul, A., et al. 2006, MNRAS, 373, 881
Pratt, G. W., Croston, J. H., Arnaud, M., & Böhringer, H. 2009, A&A, 498, 361
Press, W. H., & Schechter, P. 1974, ApJ, 187, 425
Reid, A. D., Hunstead, R. W., Lemonon, L., & Pierre, M. M. 1999, MNRAS, 302, 571
Rossetti, M., Gastaldello, F., Eckert, D., et al. 2017, MNRAS, 468, 1917
Rudnick, L., Delain, K. M., & Lemmerman, J. A. 2006, Astron. Nachr., 327, 549
Russell, H. R., van Weeren, R. J., Edge, A. C., et al. 2011, MNRAS, 417, L1
Santos, J. S., Rosati, P., Tozzi, P., et al. 2008, A&A, 483, 35
Savini, F., Bonafede, A., Brüggen, M., et al. 2018, MNRAS, 478, 2234
Savini, F., Bonafede, A., Brüggen, M., et al. 2019, A&A, 622, A24
Scaife, A. M. M., & Heald, G. H. 2012, MNRAS, 423, L30
Shakouri, S., Johnston-Hollitt, M., & Pratt, G. W. 2016a, MNRAS, 459, 2525
Shakouri, S., Johnston-Hollitt, M., & Dehghan, S. 2016b, MNRAS, 458, 3083
Shimwell, T. W., Tasse, C., Hardcastle, M. J., et al. 2019, A&A, 622, A1
Skrutskie, M. F., Cutri, R. M., Stiening, R., et al. 2006, AJ, 131, 1163
Sommer, M. W., & Basu, K. 2014, MNRAS, 437, 2163
Sommer, M. W., Basu, K., Intema, H., et al. 2017, MNRAS, 466, 996
Vacca, V., Govoni, F., Murgia, M., et al. 2011, A&A, 535, A82
van Weeren, R. J., Brüggen, M., Röttgering, H. J. A., et al. 2011, A&A, 533, A35
van Weeren, R. J., Fogarty, K., Jones, C., et al. 2013, ApJ, 769, 101
van Weeren, R. J., de Gasperin, F., Akamatsu, H., et al. 2019, Space Sci. Rev., 215, 16
Ventimiglia, D. A., Voit, G. M., Donahue, M., & Ameglio, S. 2008, ApJ, 685, 118
Venturi, T., Giacintucci, S., Brunetti, G., et al. 2007, A&A, 463, 937
Venturi, T., Giacintucci, S., Dallacasa, D., et al. 2008, A&A, 484, 327
Venturi, T., Rossetti, M., Brunetti, G., et al. 2017, A&A, 603, A125
Weißmann, A., Böhringer, H., Šuhada, R., & Ameglio, S. 2013, A&A, 549, A19
Wilber, A., Brüggen, M., Bonafede, A., et al. 2018, MNRAS, 473, 3536
Willott, C. J., Rawlings, S., Jarvis, M. J., & Blundell, K. M. 2003, MNRAS, 339, 173
ZuHone, J. A., Markevitch, M., Brunetti, G., & Giacintucci, S. 2013, ApJ, 762, 78
ZuHone, J. A., Brunetti, G., Giacintucci, S., & Markevitch, M. 2015, ApJ, 801, 146

Appendix A: Images of clusters without diffuse emission

These are images of clusters without diffuse emission.

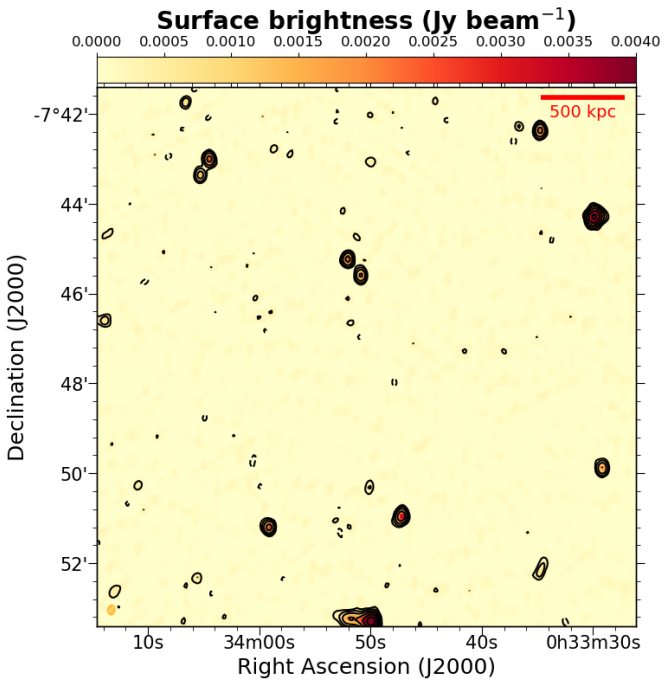

Fig. A.1. A56 JVLA C array 1.5 GHz image. Contours start at 3-$\sigma_{\rm rms}$ and are spaced by a factor of two. 1-$\sigma_{\rm rms}$ = 0.08 mJy beam^{-1} with beam = 13.″ × 10.4″.

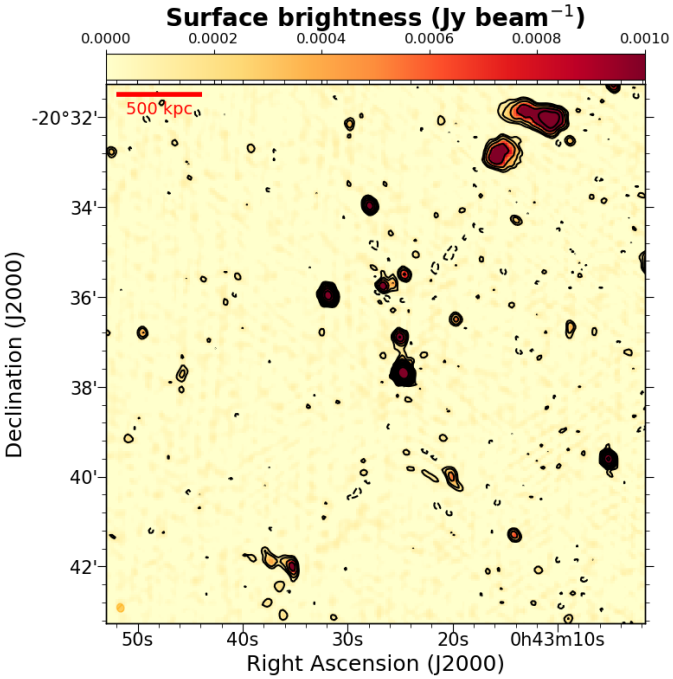

Fig. A.2. A2813 JVLA C array 1.5 GHz image. Contours start at 3-$\sigma_{\rm rms}$ and are spaced by a factor of two. 1-$\sigma_{\rm rms}$ = 0.035 mJy beam^{-1} with beam = 11.4″ × 9.5″.

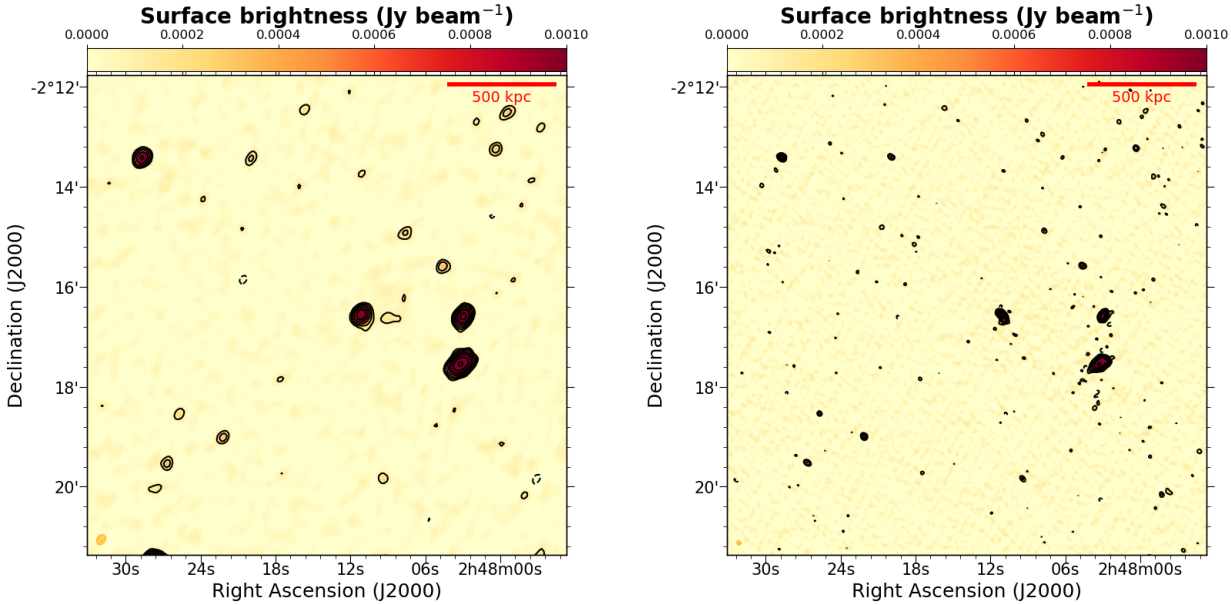

Fig. A.3. Images of the cluster A384. *Left panel*: JVLA C array 1.5 GHz image. Contours start at 3-$\sigma_{\rm rms}$ and are spaced by a factor of two. 1-$\sigma_{\rm rms}$ = 0.035 mJy beam^{-1} with beam = 13.5″ × 10.4″. *Right panel*: GMRT 610 MHz image. Contours start at 3-$\sigma_{\rm rms}$ and are spaced by a factor of two. 1-$\sigma_{\rm rms}$ = 0.05 mJy beam^{-1} with beam = 5.9″ × 4.8″.

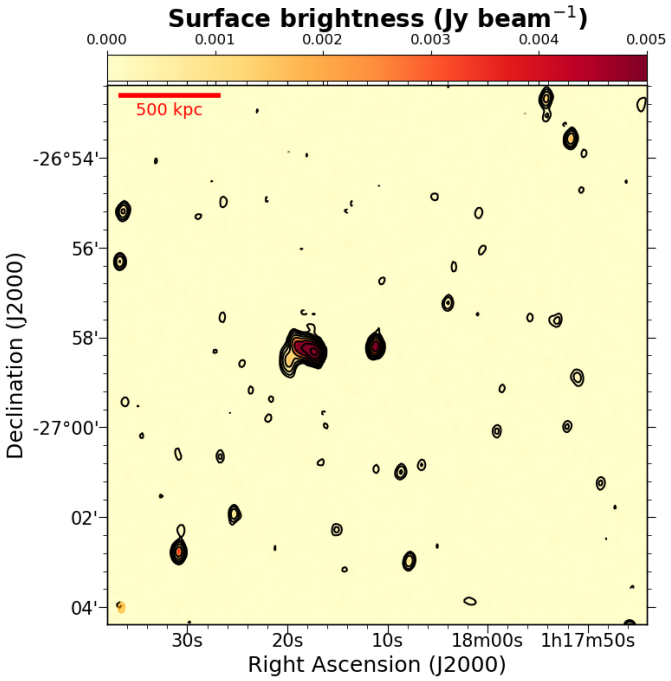

Fig. A.4. A2895 JVLA C array 1.5 GHz image. Contours start at 3-$\sigma_{\rm rms}$ and are spaced by a factor of 2. 1-$\sigma_{\rm rms}$ = 0.04 mJy beam^{-1} with beam = 14.6″ × 9.0″.

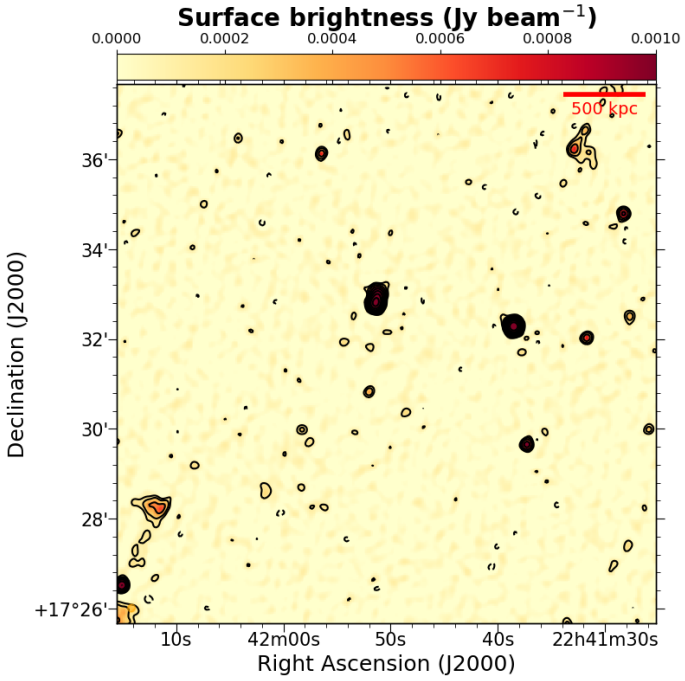

Fig. A.6. A2472 JVLA C array 1.5 GHz image. Contours start at 3-$\sigma_{\rm rms}$ and are spaced by a factor of two. 1-$\sigma_{\rm rms}$ = 0.04 mJy beam^{-1} with beam = 10.5″ × 10.1″.

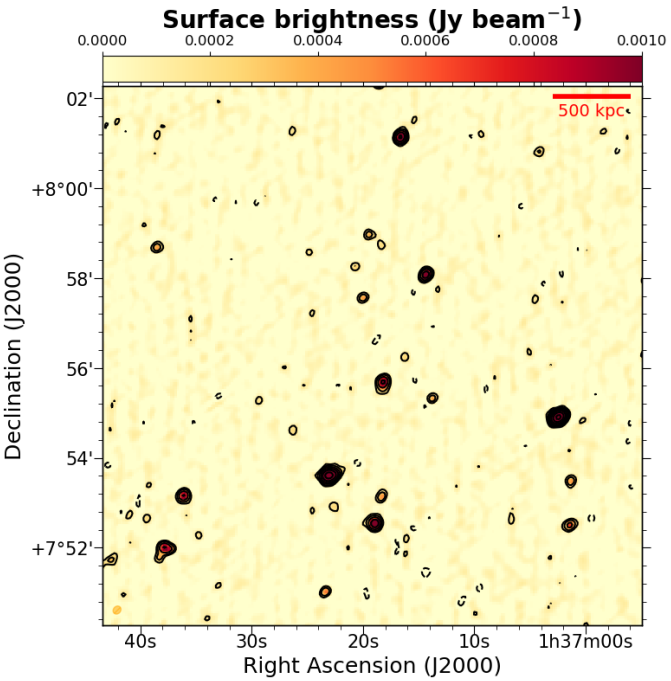

Fig. A.5. A220 JVLA C array 1.5 GHz image. Contours start at 3-$\sigma_{\rm rms}$ and are spaced by a factor of two. 1-$\sigma_{\rm rms}$ = 0.045 mJy beam^{-1} with beam = 11.6″ × 9.8″.

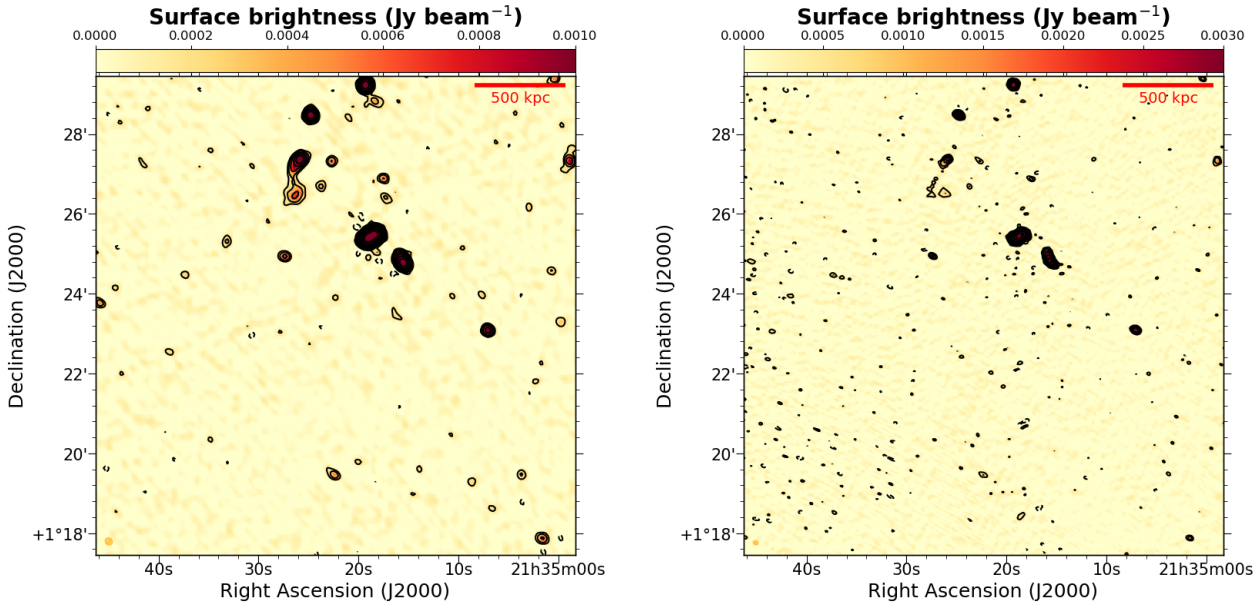

Fig. A.7. Images of the cluster A2355. *Left panel*: JVLA C array 1.5 GHz image. Contours start at 3-$\sigma_{\rm rms}$ and are spaced by a factor of two. 1-$\sigma_{\rm rms}$ = 0.04 mJy beam^{-1} with beam = 11.6″ × 10.8″. *Right panel*: GMRT 610 MHz image. Contours start at 3-$\sigma_{\rm rms}$ and are spaced by a factor of two. 1-$\sigma_{\rm rms}$ = 0.13 mJy beam^{-1} with beam = 8.3″ × 6.1″.

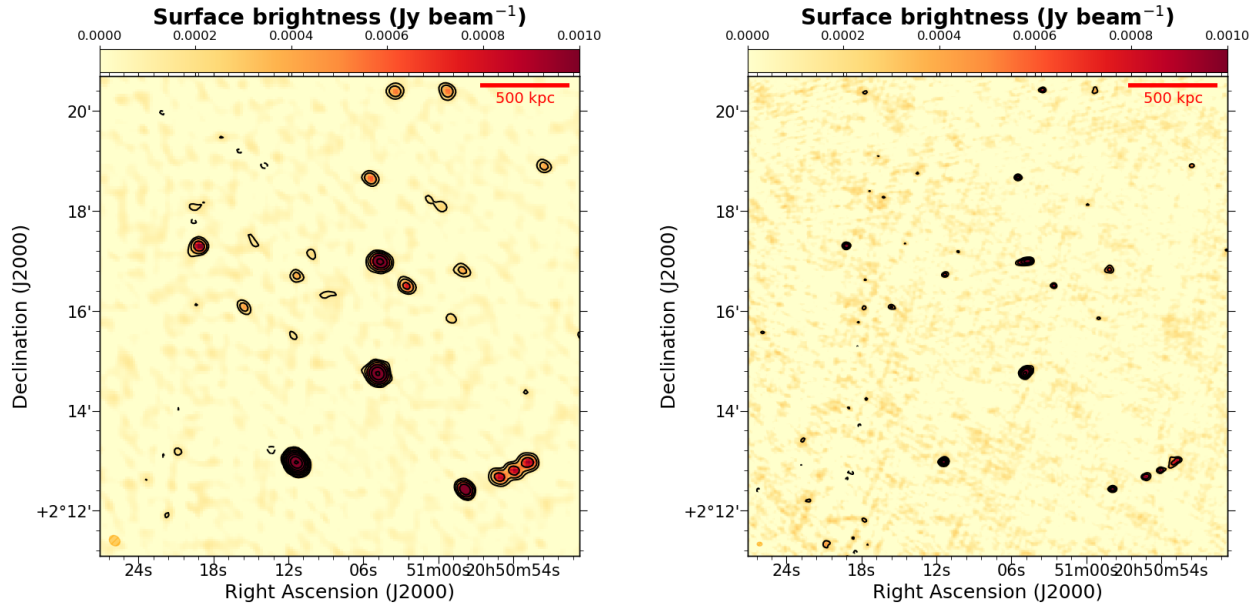

Fig. A.8. Images of the cluster RXC J2051.1+0216. *Left panel*: JVLA C array 1.5 GHz image. Contours start at 3-$\sigma_{\rm rms}$ and are spaced by a factor of two. 1-$\sigma_{\rm rms}$ = 0.05 mJy beam^{-1} with beam = 14.1″ × 11.5″. *Right panel*: GMRT 610 MHz image. Contours start at 3-$\sigma_{\rm rms}$ and are spaced by a factor of two. 1-$\sigma_{\rm rms}$ = 0.1 mJy beam^{-1} with beam = 6.0″ × 4.8″.

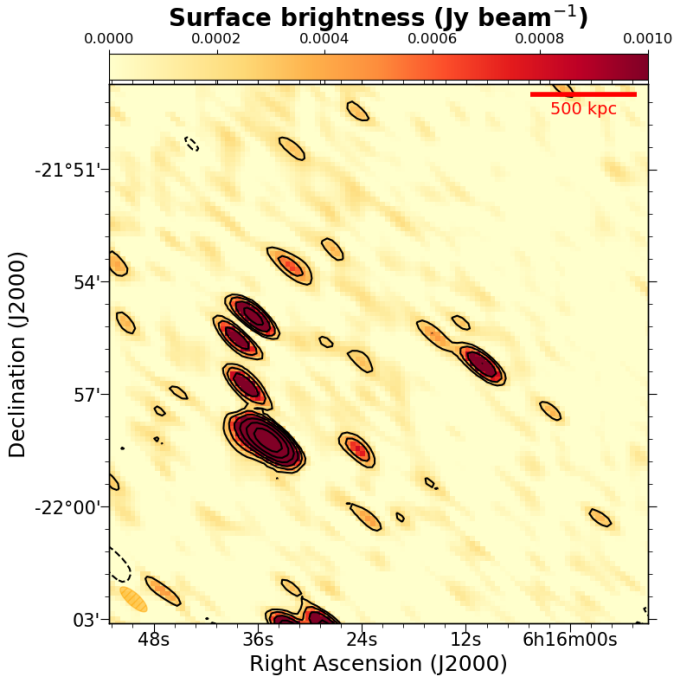

Fig. A.9. RXC J0616.3–2156 JVLA DnC array 1.5 GHz image. Contours start at 3-$\sigma_{\rm rms}$ and are spaced by a factor of 2.1-$\sigma_{\rm rms}$ = 0.08 mJy beam^{-1} with beam = 55.4″ × 19.9″.

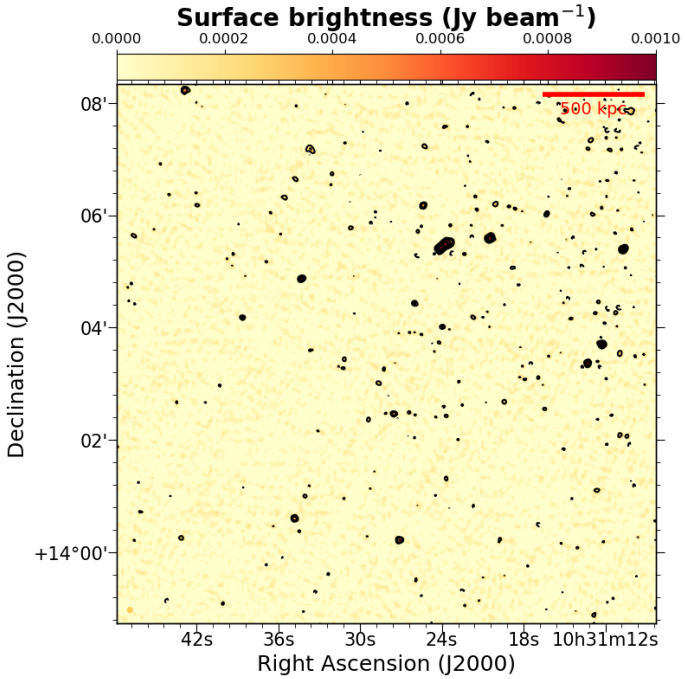

Fig. A.10. Zwcl 1028.8+1419 GMRT 610 MHz image. Contours start at 3-$\sigma_{\rm rms}$ and are spaced by a factor of wo. 1-$\sigma_{\rm rms}$ = 0.056 mJy beam^{-1} with beam = 5.3″ × 4.8″.

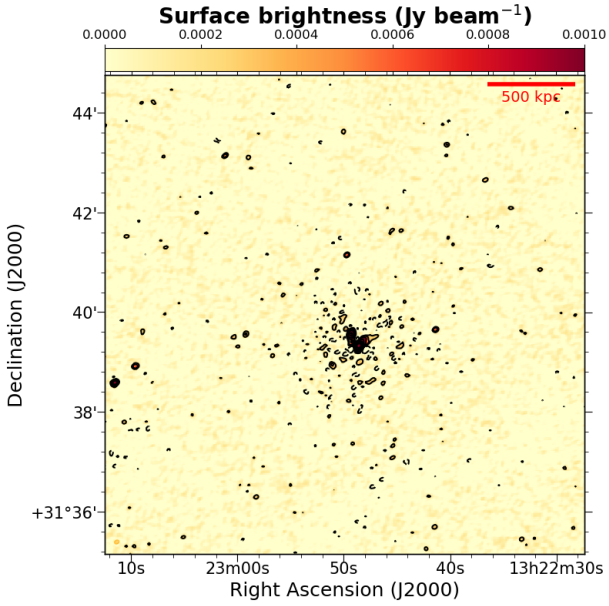

Fig. A.11. RXC J1322.8+3138 GMRT 610 MHz image. Contours start at 3-$\sigma_{\rm rms}$ and are spaced by a factor of two. 1-$\sigma_{\rm rms}$ = 0.06 mJy beam^{-1} with beam = 5.7″ × 4.4″.

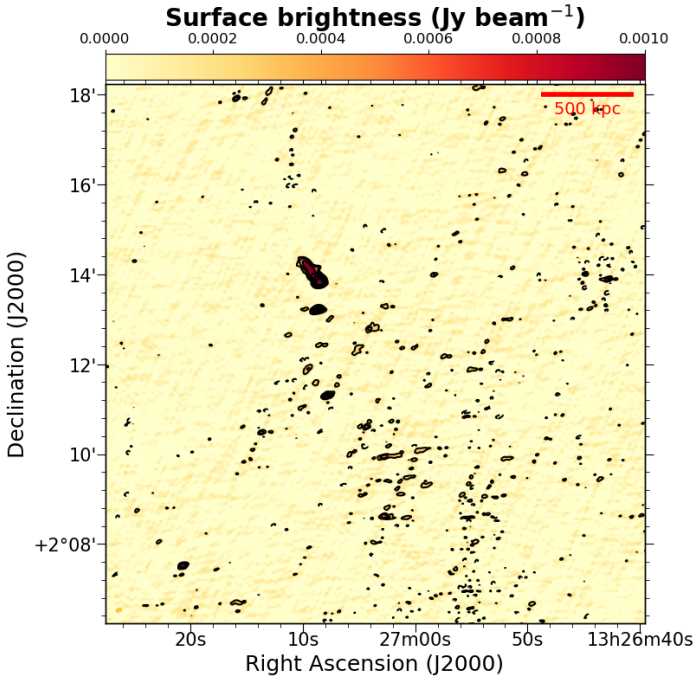

Fig. A.12. A1733 GMRT 610 MHz image. Contours start at 3-$\sigma_{\rm rms}$ and are spaced by a factor of two. 1-$\sigma_{\rm rms}$ = 0.06 mJy beam^{-1} with beam = 7.9″ × 5.0″.

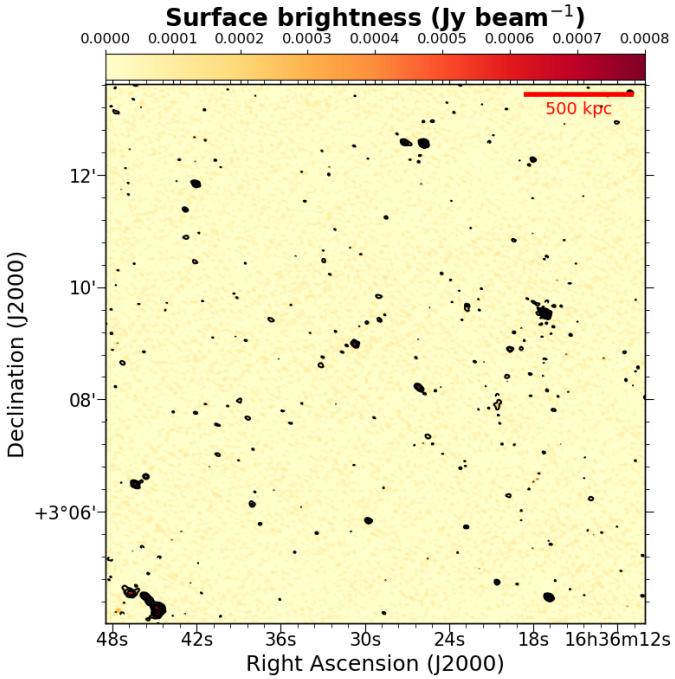

Fig. A.13. PSZ1 G019.12+3123 GMRT 610 MHz image. Contours start at 3-$\sigma_{\rm rms}$ and are spaced by a factor of two. 1-$\sigma_{\rm rms}$ = 0.035 mJy beam^{-1} with beam = 5.0″ × 3.8″.

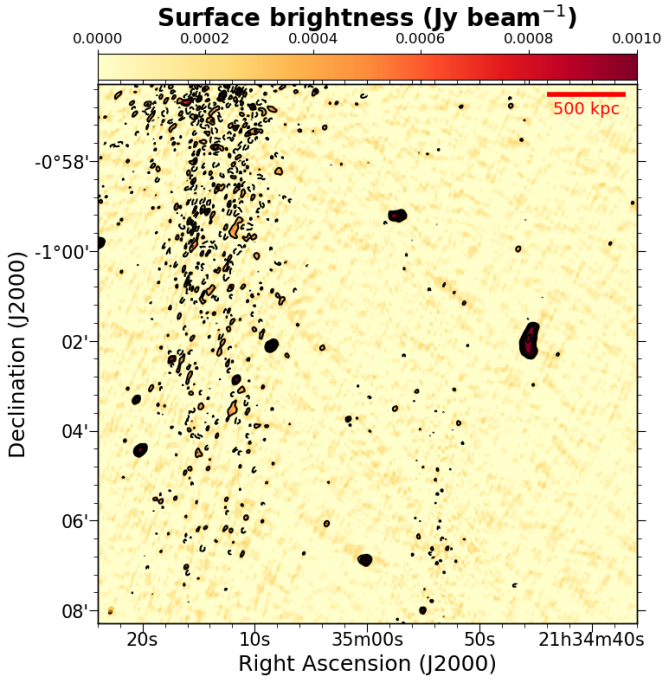

Fig. A.14. MACS J2135-010 GMRT 610 MHz image. Contours start at 3-$\sigma_{\rm rms}$ and are spaced by a factor of two. 1-$\sigma_{\rm rms}$ = 0.08 mJy beam^{-1} with beam = 7.8″ × 5.8″.

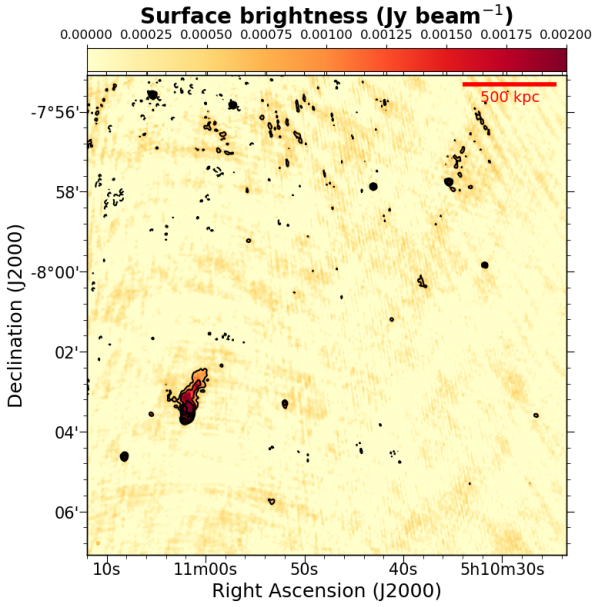

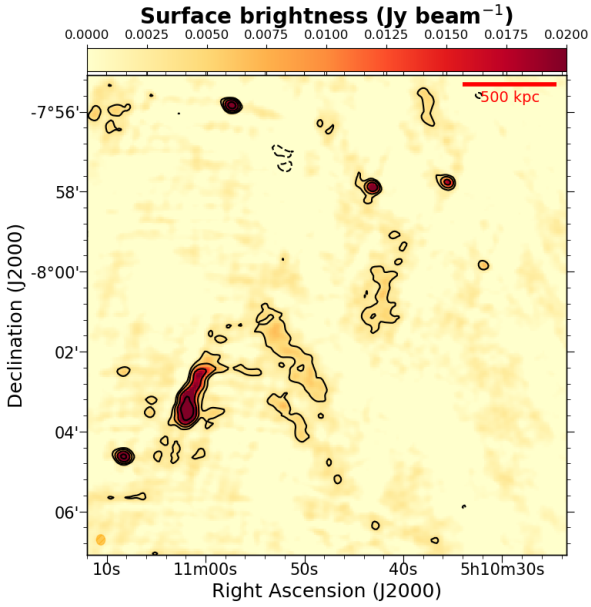

Fig. A.15. Images of the cluster RXC J0510.7–0801. *Left panel*: GMRT 610 MHz image. Contours start at 3-$\sigma_{\rm rms}$ and are spaced by a factor of two. 1-$\sigma_{\rm rms}$ = 0.2 mJy beam^{-1} with beam = 5.4 × 4.8. *Right panel*: RXC J0510.7–0801 GMRT 240 MHz image. Contours start at 3-$\sigma_{\rm rms}$ and are spaced by a factor of two. 1-$\sigma_{\rm rms}$ = 1.2mJy beam^{-1} with beam = 15.7″ × 13.1″.

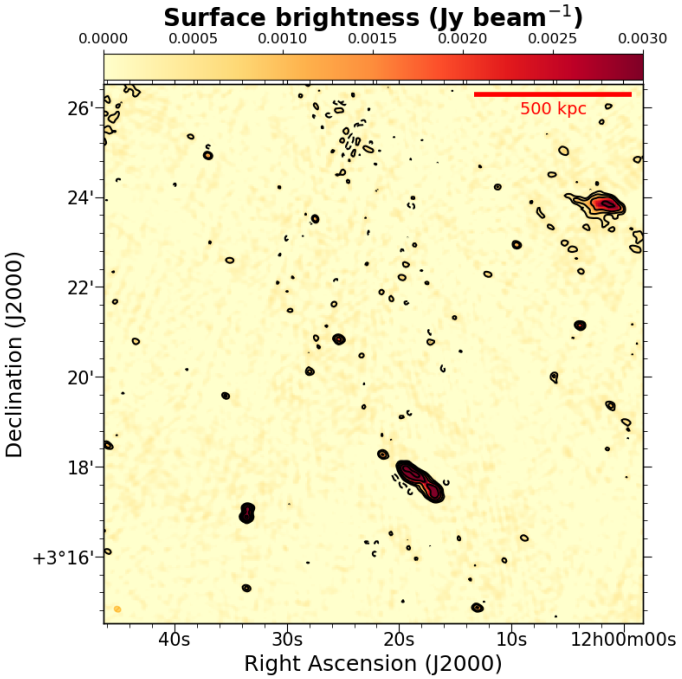

Fig. A.16. A1437 GMRT 330 MHz image. Contours start at 3-$\sigma_{\rm rms}$ and are spaced by a factor of two. 1-$\sigma_{\rm rms}$ = 0.4 mJy beam^{-1} with beam = 9.0″ × 7.4″.

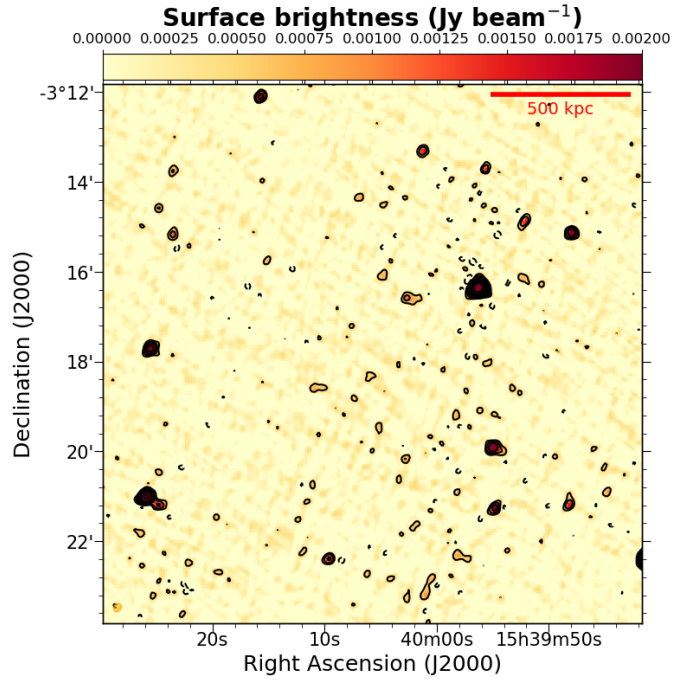

Fig. A.17. A2104 GMRT 240 MHz image. Contours start at 3-$\sigma_{\rm rms}$ and are spaced by a factor of two. 1-$\sigma_{\rm rms}$ = 0.13 mJy beam^{-1} with beam = 13.3″ × 10.4″.

Appendix B: Radio halo surface brightness radial profiles

The properties of the radio images used to derive the surface brightness radial profiles shown in Figs. B.1–B.12 are listed in Table B.1. We analysed 1.4 GHz data from the VLA archive for the clusters marked with an asterisk in the column 'Reference' of Table B.1, that is to say, A773 (project AF349), A665 (AG690, AF304), A209 (AG639), A2218 (AG344), A2744 (AF349) and A2219 (AF367, AF372). Each field was observed with both the C-array and D-array configurations. We calibrated each configuration dataset separately using AIPS, following the standard calibration scheme, with amplitude and phase calibration carried out using the primary and secondary calibration sources. The flux density scale was set using the Perley & Butler (2013) coefficients. We applied phase-only self-calibration to each dataset and produced the final images using the multi-scale CLEAN algorithm in the IMAGR task. After self-calibration, we combined the C- and D-configuration data into a single dataset for each cluster. A final cycle of phase-only self-calibration was applied to the combined datasets to improve the quality of the final images.

For each cluster, we first identified the discrete radio sources in (or projected onto) and around the cluster region using the higher-resolution images from the C-array datasets alone. We subtracted the discrete sources from the *uv*-data using the same procedure outlined in Sect. 3.1 and used the resulting datasets to obtain images of the diffuse radio emission at low-resolution using the multi-scale CLEAN. The angular resolution and noise levels of our final radio halo images are listed in Table B.1.

Table B.1. Images for surface brightness radial profiles.

Name	Telescope	ν (MHz)	Beam $FWHM$ (arcsec)	rms (mJy/beam)	Reference
A773	VLA	1400	65	0.08	*
A665	VLA	1400	65	0.16	*
A209	VLA	1400	70	0.08	*
A2163	VLA	1400	60	0.10	Rojas et al. (in prep.)
A2218	VLA	1400	50	0.05	*
A2744	VLA	1400	50	0.11	*
Z0634	JVLA	1400	40	0.08	Cuciti et al. (2018)
A2219	VLA	1400	50	0.10	*
A1758	VLA	1400	45	0.08	Botteon et al. (2018)
A697	GMRT	327	48	1.10	Macario et al. (2010)
RXC J1314.4–2515	GMRT	610	21	0.07	Venturi et al. (2007)
A521	GMRT	235	40	0.17	Brunetti et al. (2008)
PSZ1 G171.96-40.64	VLA	1400	50	0.17	Giacintucci et al. (2013)
RXC J0142.0+2131	LOFAR	144	25	0.30	Savini et al. (2019)

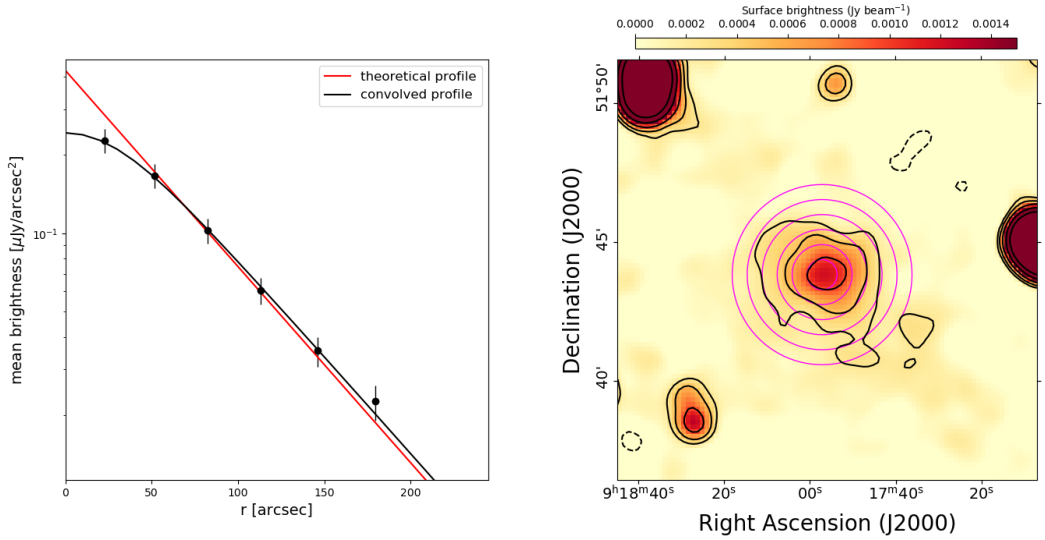

Fig. B.1. Radial surface brightness profile of the radio halo in A773. *Left*: data points represents the averaged surface brightness measured in the magenta annuli shown in the right panel. The red curve is the theoretical exponential profile and the black curve is the profile convolved with the beam of the image. *Right*: radio image of A773 (see Table B.1). Contours start at 3-σ rms noise and are spaced by a factor of two. The orange circle in the bottom left corner shows the size of the beam.

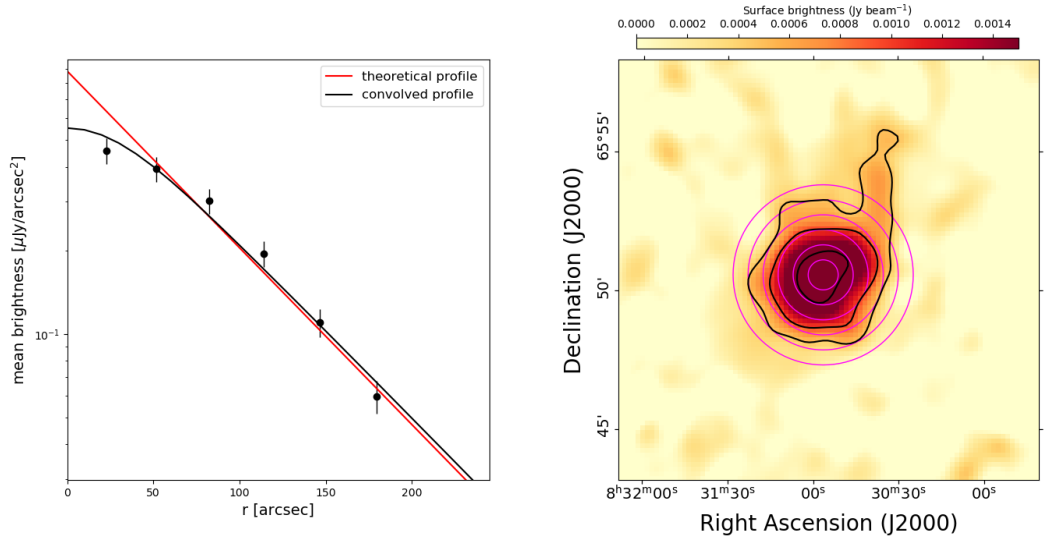

Fig. B.2. Same as Fig. B.1 for A665.

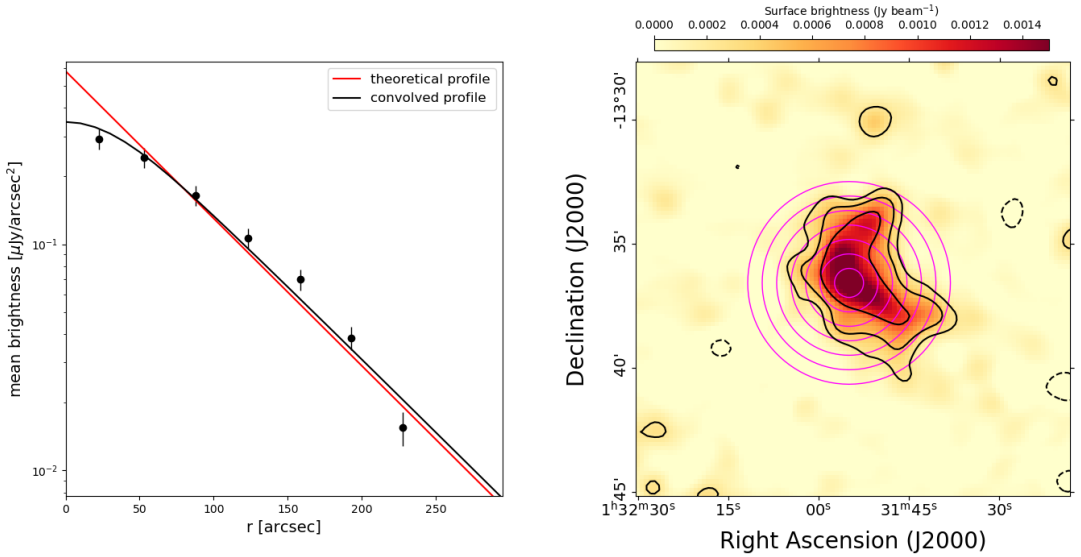

Fig. B.3. Same as Fig. B.1 for A209.

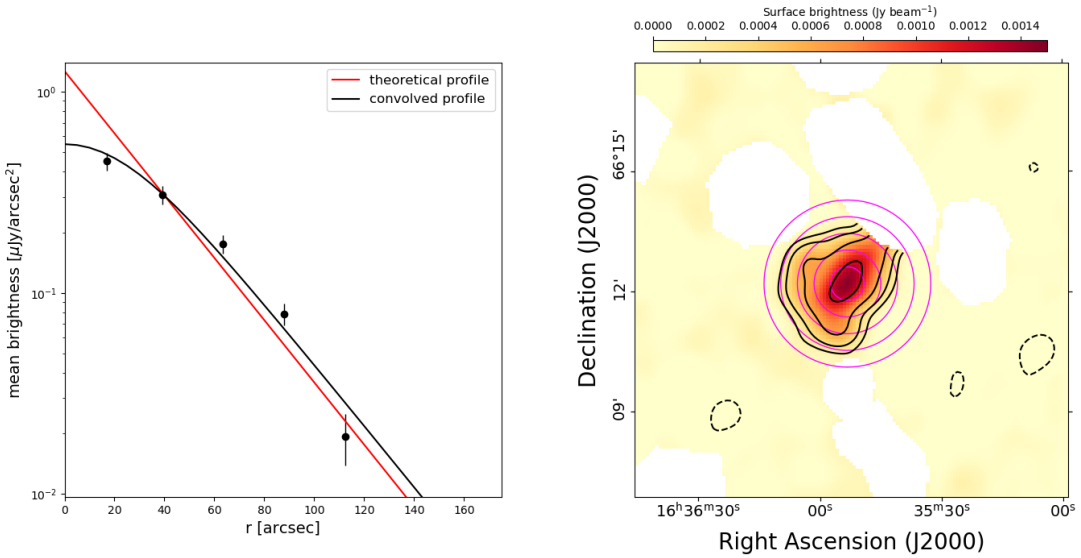

Fig. B.4. Same as Fig. B.1 for A2218.

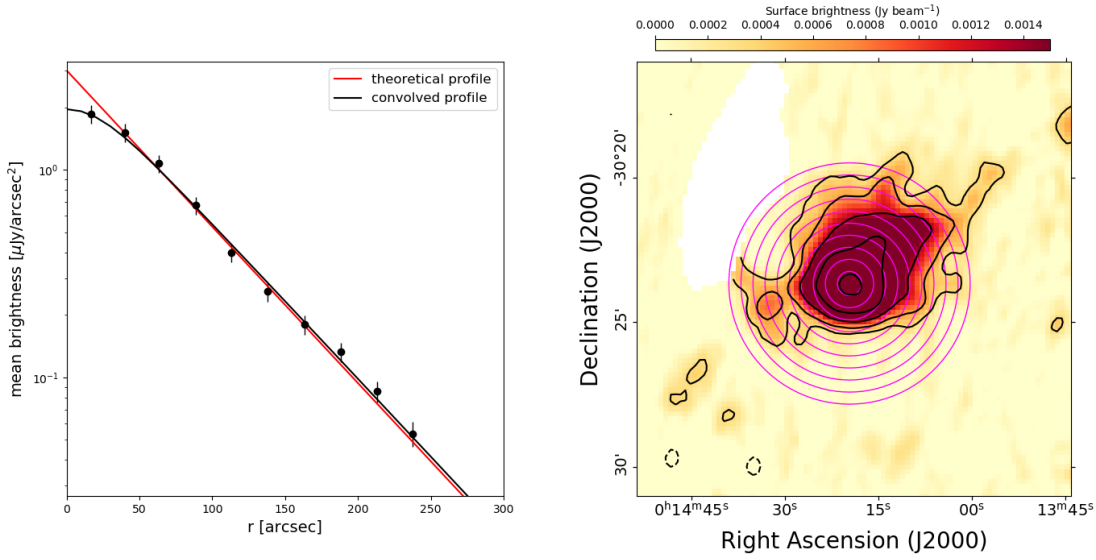

Fig. B.5. Same as Fig. B.1 for A2744.

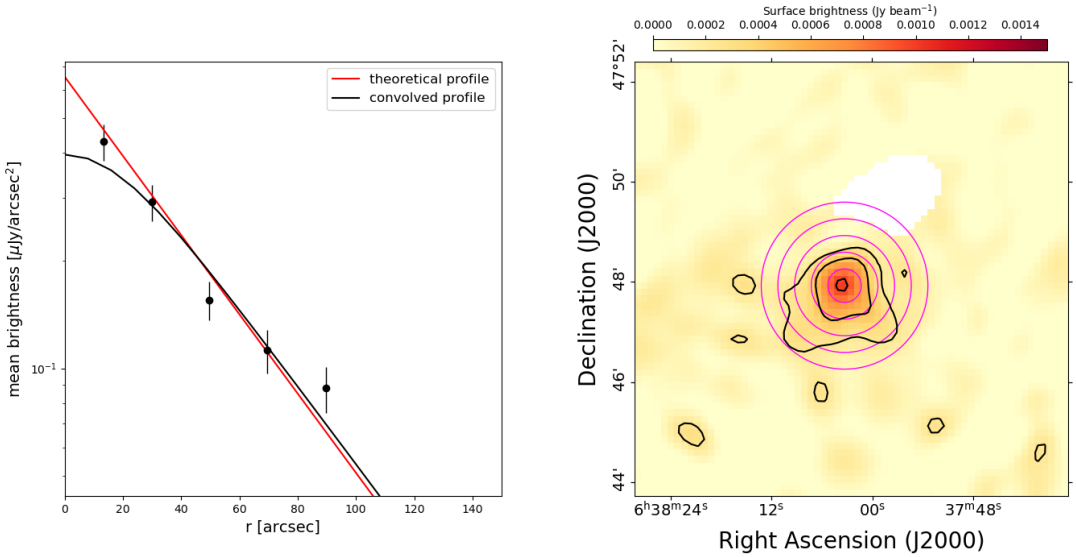

Fig. B.6. Same as Fig. B.1 for Z0634.

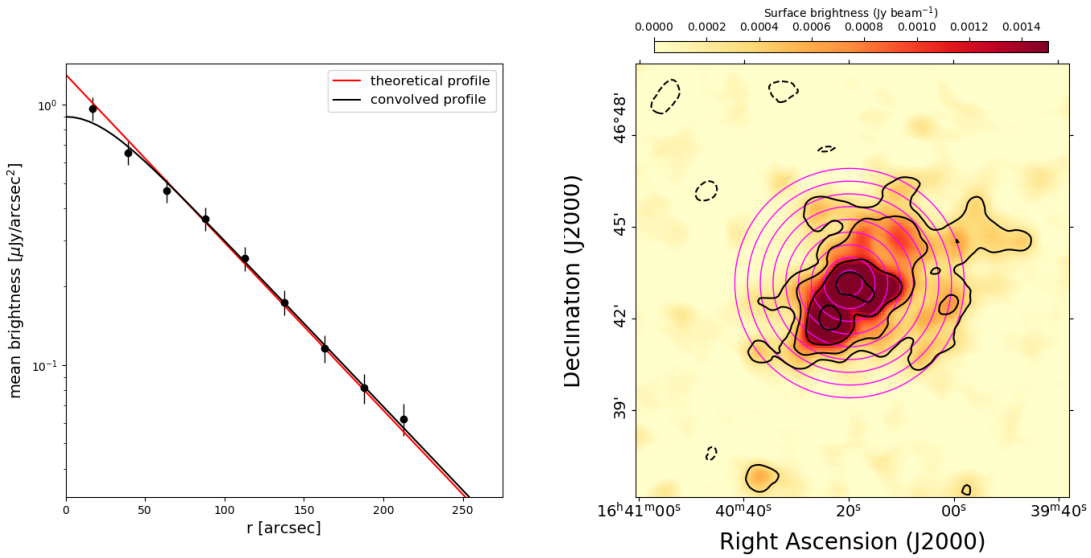

Fig. B.7. Same as Fig. B.1 for A2219.

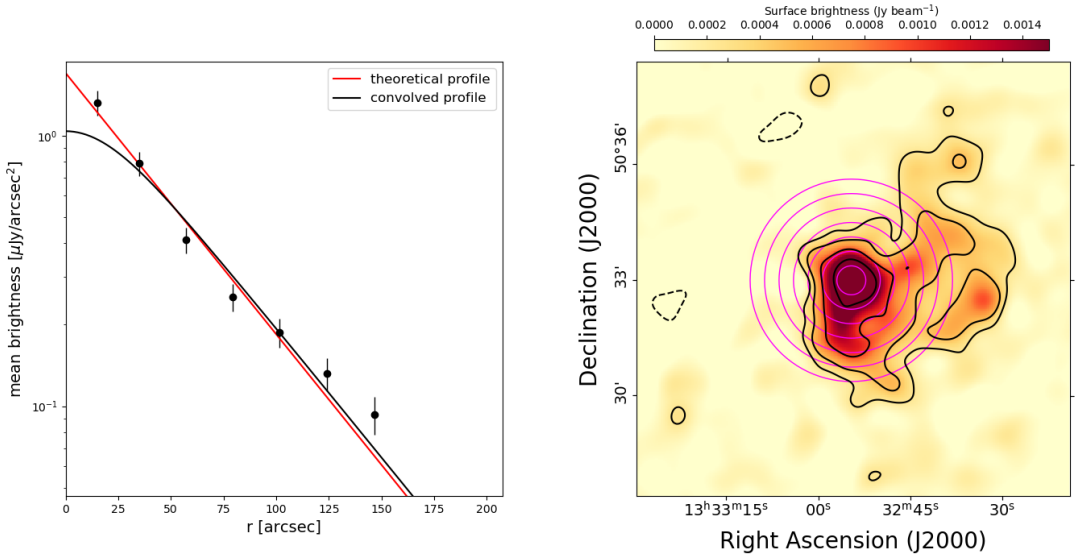

Fig. B.8. Same as Fig. B.1 for A1758.

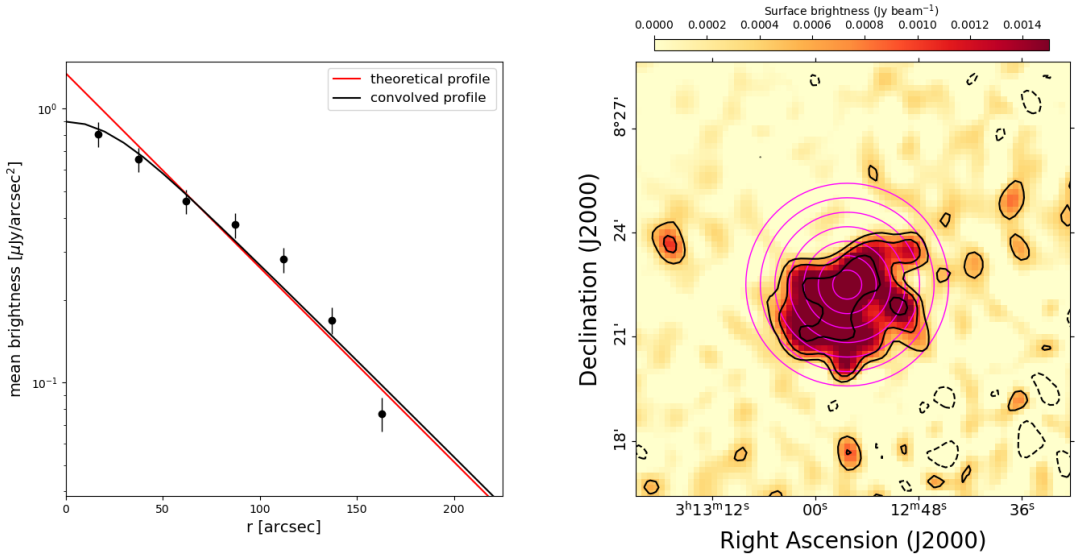

Fig. B.9. Same as Fig. B.1 for PSZ1 G171.96-40.64.

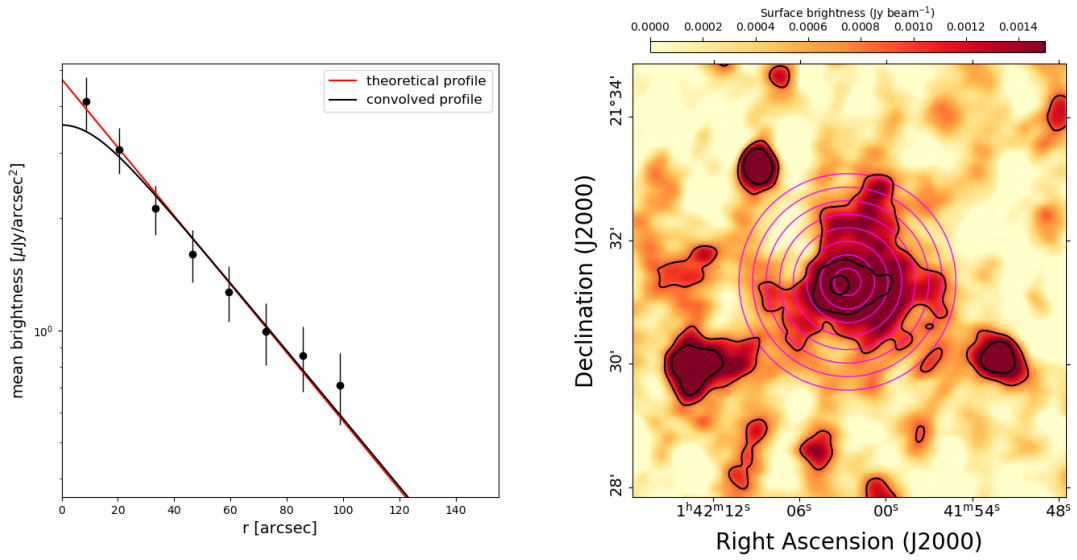

Fig. B.10. Same as Fig. B.1 for RXC J0142.0+2131.

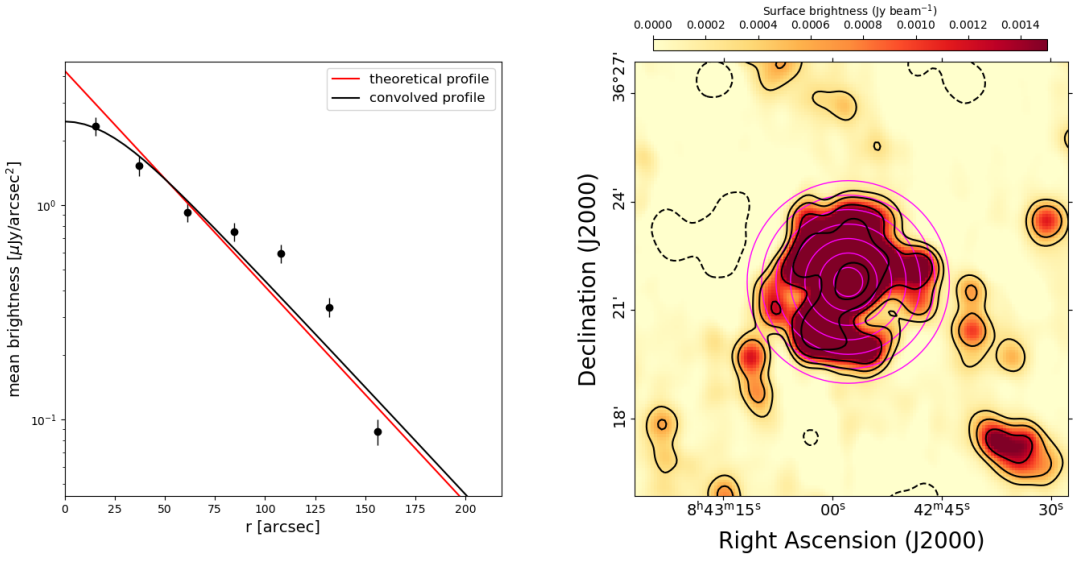

Fig. B.11. Same as Fig. B.1 for A697.

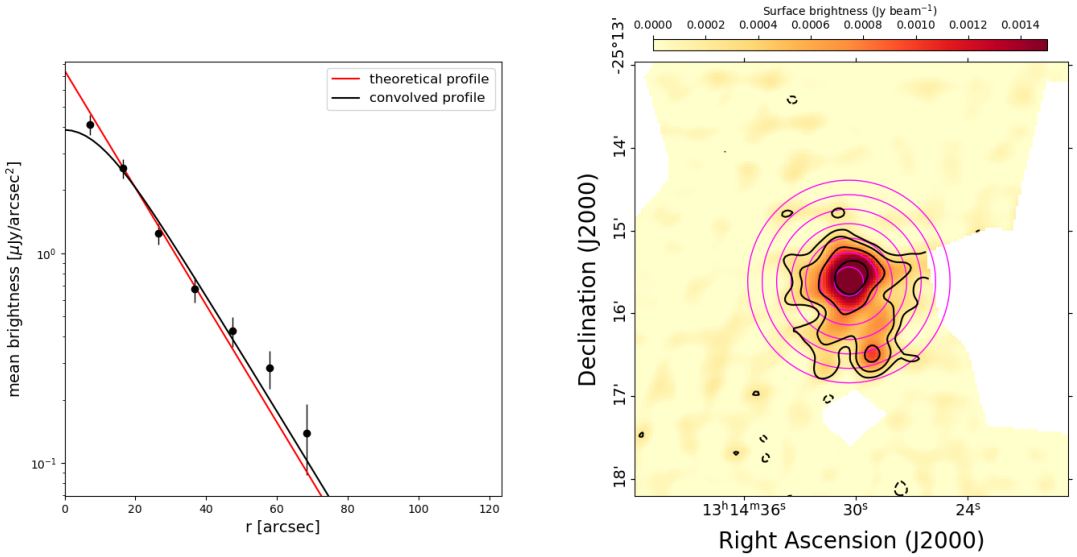

Fig. B.12. Same as Fig. B.1 for RXC J1314.4–2515.

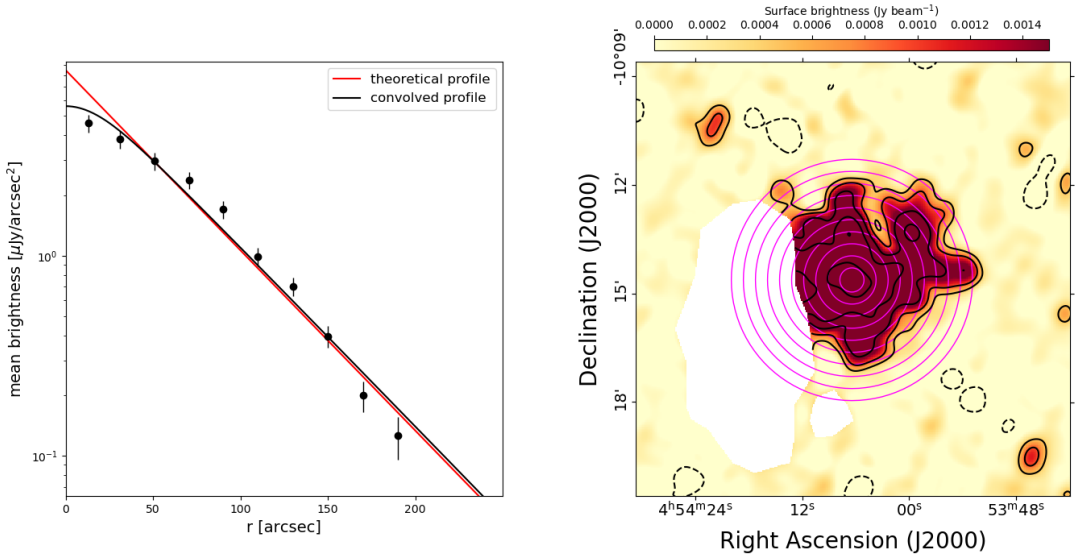

Fig. B.13. Same as Fig. B.1 for A521.